

# A deterministic adjoint-based semi-analytical algorithm for fast response change computations in proton therapy

Tiberiu Burlacu<sup>1,2</sup>, Danny Lathouwers<sup>\*1,2</sup>, and Zoltán Perkó<sup>\*1,2</sup>

<sup>1</sup>Delft University of Technology, Faculty of Applied Sciences, Delft, The Netherlands

<sup>2</sup>HollandPTC consortium<sup>†</sup>, Delft, The Netherlands

August 26, 2022

## Abstract

In this paper we propose a solution to the need for a fast particle transport algorithm in Online Adaptive Proton Therapy capable of cheaply, but accurately computing the changes in patient dose metrics as a result of changes in the system parameters. We obtain the proton phase-space density through the product of the numerical solution to the one-dimensional Fokker-Planck equation and the analytical solution to the Fermi-Eyges equation. Moreover, a corresponding adjoint system was derived and solved for the adjoint flux. The proton phase-space density together with the adjoint flux and the metric (chosen as the energy deposited by the beam in a variable region of interest) allowed assessing the accuracy of our algorithm to different perturbation ranges in the system parameters and regions of interest. The algorithm achieved negligible errors ( $1.1 \times 10^{-6} \%$  to  $3.6 \times 10^{-3} \%$ ) for small perturbation ranges ( $-40$  HU to  $40$  HU) and small to moderate errors ( $3 \%$  to  $17 \%$ ) – in line with the well-known limitation of adjoint approaches – for large perturbation ranges ( $-400$  HU to  $400$  HU) in the case of most clinical interest where the region of interest surrounds the Bragg peak. Given these results coupled with the capability of further improving the timing performance it can be concluded that our algorithm presents a viable solution for the specific purpose of Online Adaptive Proton Therapy.

---

<sup>\*</sup>Both authors contributed equally

<sup>†</sup>HollandPTC consortium – Erasmus Medical Center, Rotterdam, Holland Proton Therapy Centre, Delft, Leiden University Medical Center (LUMC), Leiden and Delft University of Technology, Delft, The Netherlands

# 1 Introduction

## 1.1 Charged particle transport

The importance of studying charged particle transport is perhaps best illustrated by its applications in a wide-ranging set of fields such as radiation protection, radiotherapy, space radiation shielding, electron and ion beam microscopy, or surface analysis and lithography [1]. The goal of charged particle transport problems is to obtain the phase-space density of particles using modelled or empirically sourced reaction cross-sections. The phase-space density of particles provides a complete description of the particle fluence and all quantities of interest that can be derived from it. To obtain a general integro-differential equation that describes the phase-space density of particles in a scattering medium the collision-free Boltzmann equation [2] is altered to account for collisions via a scatter term. This equation is Boltzmann’s general transport equation and for most realistic applications its solution is highly complex.

In practice several application-dependent approximations are applied to the Boltzmann equation in order to obtain an analytical or numerical solution, with each approaches having their individual trade-offs. For example, while Monte Carlo (MC) methods have as advantages high precision and an ease of understanding, their main disadvantage is the slow computation times which deem them inapplicable in many scenarios [1], especially when (near) real-time calculations are necessary [3]. Diametrically opposite to MC methods from a computational expense standpoint are analytical methods such as the pencil beam approaches, which are obtained through fits and approximations. As expected, these methods trade-off the high precision for the low computational expense. In between these two extremes lie several numerical or semi-numerical approaches, such as the moment method or the phase space time evolution method [4].

The focus of this paper is on a combination of numerical and analytical methods (the pencil beam and energy straggling methods) that are deemed promising for fulfilling the needs of our specific application, so called online adaptive proton therapy, which is currently the state-of-the-art form of radiotherapy.

## 1.2 Particle Transport Needs In Online Adaptive Proton Therapy

Within the field of radiation therapy, proton therapy (PT) has emerged as an alternative to conventional photon radiotherapy for cancer treatment due to its promises of increased dose conformity and lowered doses achievable in healthy tissues [5]. These benefits are due to the presence of the Bragg peak (BP) in the depth-dose distribution, as charged particles deposit most of their energy within a small volume near the end of their range. The Bragg peak however also makes proton doses highly susceptible to uncertainties [6, 7]. Some of the common sources of range uncertainties are related to CT imaging, treatment delivery or changes in the anatomy of the patient [8].

Currently, the state-of-the-art in dealing with uncertainties in clinical practice is to apply robust optimization [9, 10]. In robust optimization irradiation plans are optimized such that they ensure good performance of the plan under even the most extreme uncertainty scenarios [11]. Due to the complexity of the potential scenarios however, certain scenarios – such as anatomical variations (e.g., weight loss over the course of typically weeks long treatments) – are typically not accounted for [12]. Most importantly, robust planning essentially enlarges the high dose volume around the tumor, increasing the dose in the surrounding healthy tissues, which in turn increases the probability of detrimental side effects [13].

The ideal solution would be to use Online Adaptive Proton Therapy (OAPT) instead. In OAPT, a daily CT scan of the patient is acquired and within 30 seconds (the time for a robotic arm to move the patient from the in-room CT scanner to the irradiation location) a new, fully re-optimized plan is created [3]. Having up-to-date anatomical information allows accurately targeting the tumor [12] without needing robust planning, leading to smaller irradiated volumes and fewer side effects. Unfortunately however, the computational expense of dose calculations and plan re-optimization [14], and the time needed for the presently mostly manual plan quality assurance (QA) [15] is far larger than 30 seconds, making such workflows currently clinically infeasible.

Fast proton transport methods that are accurate in highly heterogeneous patient geometries are key to overcome these computational and QA related bottlenecks, and represent one of the missing enabling technology for online adaptive workflows and further improving cancer treatments. First, they are necessary for re-optimization, as plan optimization requires the dose distribution from each of the typically hundreds or even thousands of individual proton beams as input [16]. Second, they are crucial

for replacing the current manual, measurement based plan QA with fast computational alternatives. Traditional plan QA measurements assess the differences between planned and delivered doses in order to ensure they are within the clinically acceptable  $\pm 3\%$  [17] range and that the irradiation delivery system functions as intended [18]. Since manual measurements are clearly infeasible in OAPT, independent dose calculation methods [19] have been proposed as a viable alternative, showing similar precision when using accurate MC transport methods [20]. As further advantage, such automated QA procedures yield clinically more relevant metrics than measurements and could potentially even increase clinical throughput and treatment accessibility [21]. While the benefits of automated QA procedures based on independent dose calculation and machine log-files (measured the outgoing radiation from the treatment machine) are clear, MC calculations [22], even when multi-threaded [21] are not fast enough to perform (near) real-time QA necessary in the OAPT workflow.

### 1.3 A Semi-Analytical Adjoint-Based Deterministic Algorithm For OAPT

To overcome these issues we propose a semi-analytical adjoint-based deterministic algorithm that could serve as (near) real-time plan QA, using machine log-files and the patient geometry. The semi-analytical component aims to provide a balance between the accuracy of MC algorithms and the speed of analytical dose calculation algorithms. The adjoint component aims to provide real-time quality assurance through efficient computations of the effect of perturbations in the system parameters (beam spatial and energy spread, its particle number or the patient geometry) on the desired clinical metrics (dose, or more complex responses).

The semi-analytical component has as a starting point, similarly to the MC algorithms, the Linear Boltzmann Equation (LBE). Through the continuous slowing down, energy straggling and Fokker-Planck approximations the LBE can be reduced to two partial differential equations (PDEs). One of the PDEs is the one-dimensional Fokker-Planck (FP) equation while the other one is the Fermi-Eyges (FE) equation. The advantage of this approach is threefold. First, the approach derives a system which is described by two PDEs. The presence of the PDEs (as opposed to for example a machine learning (ML) based dose engine [23]) allows the application adjoint methods. Using functional analysis an adjoint system can be derived which can be used to avoid the expensive process of re-computing the solution to the two PDEs for each new set of system parameters. Second, the physical approximation will not suffer from the typical drawbacks of ML models such as out-of-distribution samples i.e. will remain accurate despite the input not being already seen by the algorithm. Third, while the one-dimensional FP equation requires a numerical solution the FE equation has a known analytical solution [24, 25]. This coupling will ensure the computational effectiveness as the lateral part of the proton flux is computed through a straightforward function evaluation.

### 1.4 Paper outline

Section 2 covers the theoretical background of reducing the LBE to two simplified PDEs. Section 3 describes the one-dimensional Fokker-Planck equation and its numerical solution while Section 4 covers the Fermi-Eyges solution. In Section 5 the application of the functional analysis framework for the derivation of the adjoint system with its associated adjoint solution is detailed, the solution methodology of the adjoint system is explained and the response change computations due to perturbations in the system parameters are given. Section 6 covers benchmarks of our own algorithm versus TOPAS and Bortfeld's algorithm and provides comparisons between the forward and adjoint computation of the response changes due to system parameter perturbations. Lastly, Section 7 contains some conclusions and future intended research directions.

## 2 The system model

The physical system under consideration is given by a proton beam irradiating the patient. This system can be characterized through the (steady-state) LBE, the validity of which for PT has been discussed by Borgers [26]. The LBE describes the proton balance in an arbitrary volume. Its derivation is obtained by equating all the gain and loss mechanisms for protons with a certain energy  $E$  in  $dE$  and direction  $\hat{\Omega}$  in  $d\hat{\Omega}$  in an arbitrary volume  $V$  with a boundary denoted by  $\partial V$  as outlined by Duderstadt & Hamilton [27]. The equation is an integro-differential equation for the proton flux ( $\varphi = vn$ ) with  $v$  the proton speed and  $n(\mathbf{r}, E, \hat{\Omega}, t)$  the angular proton density,

$$\hat{\Omega} \cdot \nabla \varphi + \Sigma_t(\mathbf{r}, E) \varphi(\mathbf{r}, E, \hat{\Omega}) = \int_{4\pi} d\hat{\Omega}' \int_0^\infty dE' \Sigma_s(E' \rightarrow E, \hat{\Omega}' \rightarrow \hat{\Omega}) \varphi(\mathbf{r}, E', \hat{\Omega}') + s(\mathbf{r}, E, \hat{\Omega}) \quad (1)$$

$$\text{BC: } \varphi(\mathbf{r}_s, E, \hat{\Omega}, t) = 0 \text{ if } \hat{\Omega} \cdot \hat{\mathbf{e}}_s < 0 \text{ with } \mathbf{r}_s \in \partial V, \quad (2)$$

where  $\Sigma_t$  is the total macroscopic cross section,  $\Sigma_s$  is the macroscopic double differential scattering cross section and  $s$  is the source of protons.

Currently, the LBE in its form is computationally expensive to solve. A first step is to divide the total  $\Sigma_t$  and scatter  $\Sigma_s$  cross sections according to the main interactions that a proton undergoes as it propagates through the medium, namely  $\Sigma_t = \Sigma_a + \Sigma_e + \Sigma_{in}$  where  $\Sigma_a$  is the catastrophic (absorption) scatter cross section,  $\Sigma_e$  is the elastic scatter cross section between the incident protons and the nuclei of tissue,  $\Sigma_{in}$  is the inelastic scatter cross section between the incident protons and atomic electrons. By doing so, Equation 1 can be written as

$$\begin{aligned} \hat{\Omega} \cdot \nabla \varphi = & \int_{4\pi} d\hat{\Omega}' \int_E^\infty dE' \Sigma_a(E' \rightarrow E, \hat{\Omega}' \rightarrow \hat{\Omega}) \varphi(\mathbf{r}, E', \hat{\Omega}') - \Sigma_a(\mathbf{r}, E) \varphi(\mathbf{r}, E, \hat{\Omega}) \\ & + \int_{4\pi} d\hat{\Omega}' \Sigma_e(\mathbf{r}, E, \hat{\Omega}' \rightarrow \hat{\Omega}) \varphi(\mathbf{r}, E, \hat{\Omega}') - \Sigma_e(\mathbf{r}, E) \varphi(\mathbf{r}, E, \hat{\Omega}) \\ & + \int_0^\infty dE' \Sigma_{in}(\mathbf{r}, E + Q \rightarrow E, \hat{\Omega}) \varphi(\mathbf{r}, E + Q, \hat{\Omega}) - \Sigma_{in}(\mathbf{r}, E) \varphi(\mathbf{r}, E, \hat{\Omega}). \end{aligned} \quad (3)$$

In this splitting it is assumed that the energy transfer in Coulomb elastic scatter interactions is negligible and that the angular deflection in Coulomb inelastic scatter interactions is negligible [1].

The next step is to apply approximations to each of the collision integrals in Equation 3. The inelastic scatter integral is approximated using the Continuous Slowing Down Approximation (CSDA) and the Energy-loss Straggling (ELS) approximation [1]. Thereafter, the Fokker-Planck approximation is applied to the elastic scatter angular integral and in the elastic scattering cross section  $\Sigma_e(E, \hat{\Omega} \cdot \hat{\Omega}')$  the energy is replaced by the depth-dependent mean energy  $E_a(z)$  [28, 1]. The catastrophic scatter integral is neglected completely with only the catastrophic scatter cross section absorption term remaining. Applying these approximations to the LBE reduces the integro-differential equation to the following PDE

$$\frac{\partial \varphi}{\partial z} + \Omega_x \frac{\partial \varphi}{\partial x} + \Omega_y \frac{\partial \varphi}{\partial y} - \frac{\partial S(\mathbf{r}, E) \varphi}{\partial E} - \frac{1}{2} \frac{\partial^2 T(\mathbf{r}, E) \varphi}{\partial E^2} + \Sigma_a(\mathbf{r}, E) \varphi - \Sigma_{tr}(E_a(z)) \left( \frac{\partial^2 \varphi}{\partial \Omega_x^2} + \frac{\partial^2 \varphi}{\partial \Omega_y^2} \right) = 0, \quad (4)$$

where  $S(\mathbf{r}, E)$  is the stopping power,  $T(\mathbf{r}, E)$  is the straggling coefficient,  $\Sigma_a$  is the absorption cross section and  $\Sigma_{tr}$  is the transport cross section. The resulting PDE is linear in the dependent variable  $\varphi$  which in turn depends on the six independent system variables  $\mathbf{r}, \hat{\Omega}, E$ .

We follow Gebäck and Asadzadeh's and write [28]

$$\varphi = \varphi_{FE}(\mathbf{r}, \hat{\Omega}) \cdot \varphi_{FP}(z, E). \quad (5)$$

Substitution in Equation 4 results in

$$\Upsilon(\varphi_{FE}) \cdot \varphi_{FP} + \varphi_{FE} \cdot 1\text{DFP}(\varphi_{FP}) = 0, \quad (6)$$

where  $\Upsilon(\varphi_{FE})$  is the Fermi-Eyges equation and  $1DFP(\varphi_{FP})$  is the one-dimensional Fokker-Planck equation. In order to avoid the trivial solution both of these equations must be set to zero. Specifically,

$$\Upsilon(\varphi_{FE}) = \frac{\partial \varphi_{FE}}{\partial z} + \Omega_x \frac{\partial \varphi_{FE}}{\partial x} + \Omega_y \frac{\partial \varphi_{FE}}{\partial y} - \Sigma_{tr}(E_a(z)) \left( \frac{\partial^2 \varphi_{FE}}{\partial \Omega_x^2} + \frac{\partial^2 \varphi_{FE}}{\partial \Omega_y^2} \right) = 0. \quad (7)$$

and

$$1DFP(\varphi_{FP}) = \frac{\partial \varphi_{FP}}{\partial z} - \frac{\partial S(E) \varphi_{FP}}{\partial E} - \frac{1}{2} \frac{\partial^2 T(E) \varphi_{FP}}{\partial E^2} + \Sigma_a(E) \varphi_{FP} = 0. \quad (8)$$

Using the solution of these two equations, the response of the system can be defined which in this case was chosen as the energy deposited in a certain region of interest (ROI). The method is applicable to other, more general, responses (defined as functionals or operators) as long as the chosen response satisfies a weak Lipschitz condition in the system state vector and parameters [29]. In the case of this work, the response  $R$  is given by

$$\begin{aligned} R(\varphi) &= - \int_{ROI} dV \int_{4\pi} d\hat{\Omega} \int_{E_{min}}^{E_{max}} dE \left[ \frac{\partial S(E) \varphi}{\partial E} + \frac{1}{2} \frac{\partial^2 T(E) \varphi}{\partial E^2} - E \Sigma_a \varphi \right] \\ &= - \int_{ROI} dV \int_{4\pi} d\hat{\Omega} \varphi_{FE} \int_{E_{min}}^{E_{max}} dE \left[ \frac{\partial S(E) \varphi_{FP}}{\partial E} + \frac{1}{2} \frac{\partial^2 T(E) \varphi_{FP}}{\partial E^2} - E \Sigma_a \varphi_{FP} \right], \end{aligned} \quad (9)$$

where in the last equality Equation 5 was employed.

### 3 Approximating the one-dimensional Fokker-Planck equation

The one-dimensional Fokker-Planck equation is a convection-diffusion equation in energy whose character is well suited for Discontinuous Galerkin (DG) methods. Consequently, its semi-discrete form was obtained using the Symmetric Interior Penalty Galerkin (SIPG). The main advantages of the SIPG method over other finite element methods (FEM) are the relative ease with which the approximating polynomial can be changed on different mesh elements, the fact that the method allows unstructured or adaptive meshes, and that the method satisfies a local energy balance (as opposed to the global energy balance satisfied by continuous Galerkin methods) [30]. The semi-discrete form was solved using the Crank-Nicholson (CN) method which is a second order accurate implicit finite difference method. The advantage of the CN method is that in a geometry that is piece-wise constant it relies on only one of the previous points (as opposed to schemes such as the Backward Differentiation Formula 2 that require two previous points for the same order of accuracy [31]).

The one-dimensional Fokker-Planck equation can be written in a more standard convection-diffusion form

$$\frac{\partial \varphi_{FP}}{\partial z} - \frac{\partial S^*(E) \varphi_{FP}}{\partial E} - \frac{\partial}{\partial E} \left( T^*(E) \frac{\partial \varphi_{FP}}{\partial E} \right) + \Sigma_a(E) \varphi_{FP} = 0, \quad (10)$$

where the modified stopping power  $S^* = S + \frac{1}{2} \frac{dT}{dE}$  and the modified straggling coefficient  $T^* = T/2$  are introduced. To simplify notation, the stars will from here on be dropped. Moreover, it is Equation 10 that will from now on be referred to as the one-dimensional Fokker-Planck equation. This equation can also be written in a short-hand form as

$$L(\alpha) \varphi = 0$$

where the vector of system parameters  $\alpha \in \mathcal{L}_2$  and the differential operator acting on the flux  $L$  are introduced as

$$L(\alpha)(\cdot) = \frac{\partial}{\partial z}(\cdot) - \frac{\partial S^*(\cdot)}{\partial E} - \frac{\partial}{\partial E} \left[ T^* \frac{\partial(\cdot)}{\partial E} \right] + \Sigma_a(\cdot),$$

and  $\alpha = (S^*(E), T^*(E), \Sigma_a(E))$ .

#### 3.1 Domain definition and discretization

The computational domain of the equation is given as  $\mathcal{D} = (0, z_{max}) \times (E_{min}, E_{max})$ ,  $\mathcal{D} \subset \mathbb{R}^2$ . The solution of the one-dimensional Fokker-Planck equation is the Fokker-Planck flux  $\varphi_{FP}(z, E) \in \mathcal{H}$  where  $\mathcal{H} = \mathcal{L}_2(\mathbb{R}^2)$  is a real Hilbert space with an associated inner product defined as

$$\langle f, g \rangle = \int_0^\infty dz \int_0^\infty dE f g.$$

To ensure a unique solution to Equation 10 boundary conditions must be imposed, namely

$$\text{BCE: } \varphi_{FP}(z, E) \Big|_{E=E_{max}} = 0, \quad \frac{\partial \varphi_{FP}(z, E)}{\partial E} \Big|_{E=E_{max}} = 0. \quad (11)$$

$$\text{BCS: } \varphi_{FP}(0, E) = A e^{-\left(\frac{E-E_0}{\sigma_E}\right)^2}. \quad (12)$$

The boundary conditions in energy (BCE) are homogeneous Dirichlet and Neumann conditions while the boundary condition in space (BCS) is given by a Gaussian function in energy. Gerbershagen [32] showed that this is a realistic energy spectrum for a proton beam that has suffered energy degradation. In line with usual practice, a rigorous proof of the existence and uniqueness of the solution to Equation 10 and its associated boundary conditions is not given and these properties are assumed to be true. The energy component of the domain  $\mathcal{D}$  is discretized into a number  $NG$  of groups. In a given group  $g$  the high energy boundary is denoted by  $E_{g-1/2}$ , the low energy one by  $E_{g+1/2}$  and the center value by  $E_g$ . Thus,  $E_{max} = E_{1/2}$  and  $E_{min} = E_{NG+1/2}$ . An illustration of this discretization can be seen in Figure 1.

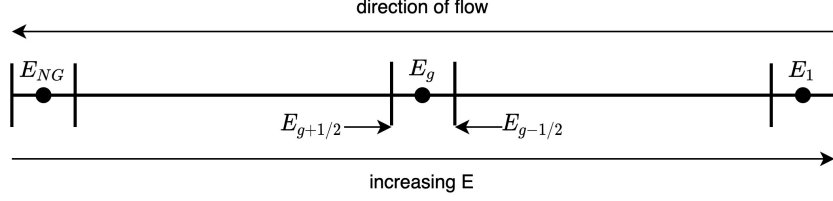


Figure 1: Energy domain discretization

The spatial part of the domain  $\mathcal{D}$  is discretized into a number of steps  $N_s$  with the interval length  $\Delta z$  allowed to vary on a per step basis and the start and end points of the spatial domain are given by  $z_0 = 0$  and  $z_{N_s} = z_{max}$ .

### 3.2 Semi-discrete variational formulation

The first step to obtain an approximation to the solution of Equation 10 and its associated boundary conditions 11, 12 is to obtain the semi-discrete variational formulation. To do so, several quantities must be defined. First, the jump and the average of the flux at the edges of an energy group are defined as

$$[\varphi] = \varphi(E_j^-) - \varphi(E_j^+),$$

$$\text{and } \{\varphi\} = \frac{1}{2}(\varphi(E_j^-) + \varphi(E_j^+)),$$

where  $j = \frac{1}{2}, \dots, NG + \frac{1}{2}$  and with  $E_j^- = \lim_{\epsilon \downarrow 0} (E_j - \epsilon)$  and  $E_j^+ = \lim_{\epsilon \downarrow 0} (E_j + \epsilon)$ . Special cases are defined at the boundary of the energy domain where

$$[v(E_{NG+1/2})] = -v(E_{NG+1/2}^+), \quad \{v(E_{NG+1/2})\} = v(E_{NG+1/2}^+), \text{ and}$$

$$[v(E_{1/2})] = v(E_{1/2}^-), \quad \{v(E_{1/2})\} = v(E_{1/2}^-).$$

Second, the penalty term is defined as

$$J_0(v, w) = \sum_{j=1/2}^{NG+1/2} \frac{\sigma^0}{h_{j-1,j}} [v(E_j)] [w(E_j)]$$

where  $h_{j-1,j} = \max(\Delta E_{j-1}, \Delta E_j)$  and  $\sigma^0$  is a real and nonnegative number bounded from below. The role of this term is to penalize the jumps in the solution.

By multiplying Equation 10 with a test function  $v$ , integrating over one group, thereafter summing over all energy groups and making use of the definitions of the jump and the average, the semi-discrete variational formulation is found to be

$$\int_{E_{min}}^{E_{max}} dE \frac{\partial \varphi_{FP}}{\partial z} v + a_{SIPG}(\varphi_{FP}, v) - \int_{E_{min}}^{E_{max}} dE \frac{\partial S^* \varphi_{FP}}{\partial E} v + \int_{E_{min}}^{E_{max}} dE \Sigma_a \varphi_{FP} v = 0, \quad (13)$$

where the SIPG bilinear  $a_{SIPG}$  is [30]

$$a_{SIPG}(\varphi_{FP}, v) = \int_{E_{min}}^{E_{max}} T \frac{\partial \varphi_{FP}}{\partial E} \frac{dv}{dE} dE + \sum_{\Gamma_i} - \left\{ T \frac{\partial \varphi_{FP}}{\partial E} \right\} \cdot [v] - [\varphi_{FP}] \cdot \left\{ T \frac{dv}{dE} \right\} + \frac{\sigma}{\Delta E} [\varphi_{FP}] [v], \quad (14)$$

where  $\Gamma_i$  denotes the interior points of the energy domain. Following Hillewaert's work [33], the penalty parameter was set as a function of the maximum polynomial degree  $\max(\deg(p_g^i))$  of the basis functions, namely

$$\sigma^0 = \frac{(\max(\deg(p_g^i)) + 1)^2}{2}. \quad (15)$$

Both a coercivity analysis and the proof of equivalence between the semi-discrete variational formulation from Equation 13 and the model problem 10 with its associated boundary conditions 11 and 12 are beyond the scope of this paper and can be found in the work of Hillewaert and Riviere respectively [33, 30].

### 3.3 Basis functions

The first three group-centered Legendre polynomials

$$p_g^i(E) \equiv P_i\left(\frac{2}{\Delta E_g}(E - E_g)\right), i = 0, 1, 2 \quad (16)$$

were used as the basis functions for the expansion of the flux in the computational domain as

$$\varphi_{FP}(z, E) = \sum_{g=1}^{NG} \sum_{i=0}^2 \varphi_g^i(z) p_g^i(E). \quad (17)$$

Introducing the expansion from Equation 17 into the semi-discrete variational formulation from Equation 13 and sequentially replacing the function  $v$  with the chosen basis functions  $p_g^i(E)$  yields a system of linear equations. This system can be written as

$$M \frac{d\Phi}{dz} + G\Phi = 0, \quad (18)$$

where  $\Phi$  is a vector with dimension  $(1 + \max(\deg(p_g^i))) \times NG$  and its elements are given by the unknown coefficients  $\varphi_g^i(z)$  from Equation 17, the mass matrix  $M$  is a diagonal matrix that in a given group  $g$  has elements  $\int dE p_g^i(E) p_g^i(E)$  with  $i = 0, 1, 2$  along the diagonal and  $G$  is the system matrix which receives contributions from the stopping power, straggling coefficient and absorption cross section discretization.

This resulting system is discretized in space using the Crank-Nicholson method. Depending on the chosen number of groups the size of the resulting system is on the order of  $10^3$ . This relatively small size of the system of equations implies that direct solution methods are comparable in computational time to iterative ones. To this end, the banded system solver DGBSV from the LAPACK library [34] was used.

Initially, the algorithm used first order basis functions. However, the resulting fluxes for coarse energy and spatial grids resulted in unphysical negative values. Thereafter, second order basis functions were implemented.



## 4 The Fermi-Eyges equation

This section describes the analytical solution to the Fermi-Eyges equation and the steps taken to implement it. This solution is based on refinements brought to Fermi's original theory on the distribution of charged particles undergoing multiple elastic scattering in their passing through matter. Authors such as Eyges, Brahme and Asadzadeh [24, 25, 28] have brought the theory into its form presented here. A full derivation from basic principles is beyond the scope of this document and can be found in the previously mentioned publications.

The Fermi-Eyges equation

$$\Upsilon[\varphi_{FE}] = \frac{\partial \varphi_{FE}}{\partial z} + \Omega_x \frac{\partial \varphi_{FE}}{\partial x} + \Omega_y \frac{\partial \varphi_{FE}}{\partial y} - \Sigma_{tr}(z) \left( \frac{\partial^2 \varphi_{FE}}{\partial \Omega_x^2} + \frac{\partial^2 \varphi_{FE}}{\partial \Omega_y^2} \right) = 0 \quad (19)$$

can be solved by separating the  $x$  and  $y$  directions, namely  $\varphi_{FE}(\mathbf{r}, \Omega_x, \Omega_y) = H(z, x, \Omega_x) \cdot H(z, y, \Omega_y)$ . This results in two separate PDEs for each direction

$$\frac{\partial H(z, \xi, \omega)}{\partial z} + \omega \frac{\partial H(z, \xi, \omega)}{\partial \xi} - \Sigma_{tr}(z) \frac{\partial^2 H(z, \xi, \omega)}{\partial \omega^2} = 0, \quad (20)$$

where  $\xi$  stands for one of  $x, y$  and  $\omega$  stands for one of  $\Omega_x, \Omega_y$ . The resulting PDEs have the same boundary condition imposed, namely

$$H(0, \xi, \omega) = C \exp \left( - (a_1 \xi^2 + a_2 \xi \omega + a_3 \omega^2) \right), \quad (21)$$

with  $a_i \in \mathbb{R}, \forall i = 1, 2, 3$  and  $C > 0$ . The solution of Equation 20 is found by applying two-dimensional Fourier transforms in  $\xi$  and  $\omega$  and accounting for the Gaussian initial condition as detailed by Eyges and Brahme [25, 24]. In doing so the solution to the Fermi-Eyges Equation 19 is found to be

$$\varphi_{FE}(z, \boldsymbol{\rho}, \hat{\boldsymbol{\Omega}}) = \frac{A^2}{4\pi^2} \frac{\exp \left( - \frac{|\boldsymbol{\rho}|^2}{2\xi^2(z)} \right) \exp \left( - \frac{1}{2B(z)} \left| \hat{\boldsymbol{\Omega}} - \frac{\overline{\theta\xi(z)}}{\xi^2(z)} \boldsymbol{\rho} \right|^2 \right)}{\xi^2(z) B(z)}, \quad (22)$$

where  $\boldsymbol{\rho} = (x, y)$ ,  $\hat{\boldsymbol{\Omega}} = (\Omega_x, \Omega_y)$  and the remaining quantities are defined as

$$B(z) = \overline{\theta^2}(z) - \frac{(\overline{\theta\xi(z)})^2}{\xi^2(z)}, \quad A = \frac{2\pi C}{D}, \quad D = 4a_1 a_3 - a_2^2.$$

Jette [35] showed that if there is any scattering at all, then  $B \geq 0$  must hold. This was used as a check that the obtained coefficient values were not spurious. The coefficients  $\overline{\theta^2}, \overline{\theta\xi}, \overline{\xi^2}$  present in the Fermi-Eyges solution are the moments of the  $\Sigma_{tr}$  transport cross section and are found from the following equations

$$\overline{\theta^2}(z) = \overline{\theta^2}(0) + \int_0^z \Sigma_{tr}(z') dz', \quad \text{with } \overline{\theta^2}(0) = \frac{2a_3}{D} \quad (23a)$$

$$\overline{\theta\xi}(z) = \overline{\theta\xi}(0) + \overline{\theta^2}(0)z + \int_0^z (z - z') \Sigma_{tr}(z') dz', \quad \text{with } \overline{\theta\xi}(0) = \frac{a_2}{D} \quad (23b)$$

$$\overline{\xi^2}(z) = \overline{\xi^2}(0) + 2\overline{\theta\xi}(0)z + \overline{\theta^2}(0)z^2 + \int_0^z (z - z')^2 \Sigma_{tr}(z') dz', \quad \text{with } \overline{\xi^2}(0) = \frac{2a_1}{D}. \quad (23c)$$

where

$$\Sigma_{tr}(z) = \int_{-1}^1 d\mu \Sigma_s(E_a(z), \mu) (1 - \mu), \quad \text{with } \mu = \cos(\hat{\boldsymbol{\Omega}} \cdot \hat{\boldsymbol{\Omega}}'), \quad (24)$$

and  $\Sigma_s$  is the macroscopic elastic scatter cross section. Gottschalk [36] showed that the FE coefficients  $\overline{\theta^2}(z)$ ,  $\overline{\xi^2}(z)$ ,  $\overline{\theta\xi}(z)$  can be interpreted as the variances of the angular direction, the lateral position and the covariance of the lateral position and the angular direction respectively.

Next to its analytical nature an important feature of the Fermi-Eyges solution from Equation 22 is that it is a Gaussian function in both the spatial and angular directions with coefficients that are determined by the average depth-dependent beam energy and the elastic scatter cross section from Equation 24 corresponding to that energy. A disadvantage of this solution is that only the average depth dependent energy instead of the full beam energy spectrum is used to calculate the coefficients. As lower energy protons tend to scatter more it is expected that only using the average beam energy will result in an underestimation of the amount of scatter that the proton beam suffers.

#### 4.1 Solution method

The coefficients of the boundary condition are chosen in such a way that Equation 21 represents the two-dimensional normal distribution. By setting the average values in  $\xi$  and  $\omega$  to zero the coefficients  $a_i, i \in [1, 2, 3]$  from Equation 21 are easily identified to be equal to

$$a_1 = \frac{1}{2(1 - \varrho^2)\sigma_\xi^2}, a_2 = -\frac{\varrho}{(1 - \varrho^2)\sigma_\xi\sigma_\omega}, a_3 = \frac{1}{2(1 - \varrho^2)\sigma_\omega^2}, \quad (25)$$

where  $\varrho$  is the correlation coefficient between the spatial dimension  $\xi$  and the angular dimension  $\omega$ ,  $\sigma_\xi$  standard deviation in  $\xi$  and  $\sigma_\omega$  standard deviation in  $\omega$ . The  $a_i$  coefficients are thereafter used to initialize the values of the FE coefficients.

To compute the FE coefficients at a given depth the average beam energy at that depth must be known. This quantity was defined as

$$E_a(z) = \frac{\int_0^\infty dE \varphi_{FP}(z, E) E}{\int_0^\infty dE \varphi_{FP}(z, E)}. \quad (26)$$

The average energy is thereafter introduced into the elastic scatter cross section via the classical relationship between speed and energy  $v_p = \sqrt{2E_a(z)/m_p}$ . The elastic scatter cross section is in turn used to compute the transport cross section from Equation 24. To compute the angle integral the QAGE routine from the QUADPACK library was used [37].

Once  $\Sigma_{tr}(z)$  is known for all the points of  $z$  dimension, the coefficients given in Equation 23 can be calculated. As  $z$  increases in the integrals from Equations 23 so do the integrands and the computational expense of these integrals. We chose to approximate  $\Sigma_{tr}$  in a given step as the average of its values at the start and endpoint of the step. In doing so, the integrals could be re-written to depend only on the previous value.

#### 4.2 The planar integral approximation

In the response computation the angle integrated FE flux is needed. In the derivation of the Fermi-Eyges solution the domain of  $\Omega_x$  and  $\Omega_y$  is extended from their normal range to the  $(-\infty, \infty)$  range in order to apply the Fourier transforms. Since the Fermi-Eyges solution is obtained through this extension, the same extension should be consistently applied throughout the calculations that involve this solution. Thus, the angular integral can be approximated to

$$\begin{aligned} \int_{4\pi} \exp\left(-\frac{1}{2B(z)}\left|\boldsymbol{\Theta} - \frac{\overline{\theta\xi}(z)}{\overline{\xi^2}(z)}\boldsymbol{\rho}\right|^2\right) \sin\theta d\theta d\phi &\approx \int_{-\infty}^{\infty} \int_{-\infty}^{\infty} \exp\left(-\frac{1}{2B(z)}\left|\boldsymbol{\Theta} - \frac{\overline{\theta\xi}(z)}{\overline{\xi^2}(z)}\boldsymbol{\rho}\right|^2\right) d\Omega_x d\Omega_y \\ &= \int_{-\infty}^{\infty} \int_{-\infty}^{\infty} \exp\left(-\frac{1}{2B(z)}\left[(\Omega_x - c_x)^2 + (\Omega_y - c_y)^2\right]\right) d\Omega_x d\Omega_y \\ &= \sqrt{2\pi B(z)} \cdot \sqrt{2\pi B(z)} = 2\pi B(z). \end{aligned} \quad (27)$$

Thus, the angularly integrated FE flux is

$$\Psi_{FE}(x, y, z) = \int_{4\pi} \varphi_{FE}(x, y, z, \Omega_x, \Omega_y) d\hat{\Omega} = \frac{A^2}{2\pi} \frac{1}{\xi^2(z)} \exp\left(-\frac{|\rho|^2}{2\xi^2(z)}\right). \quad (28)$$

### 4.3 Data sources

In order to obtain the solution to the two PDEs and the response, the stopping power, straggling coefficient, absorption cross section and elastic scatter cross section must be known as a function of energy and tissue composition. The CT scan HU values were converted to density and fractional compositions according to Schneider's method [38]. The density and fractional composition were used to interpolate nuclide specific tables of the stopping power versus energy. The tables were extracted from TOPAS [39] using an adapted extension distributed on the TOPAS forum [40]. The stopping power for protons in water versus energy can be seen in Figure 2.

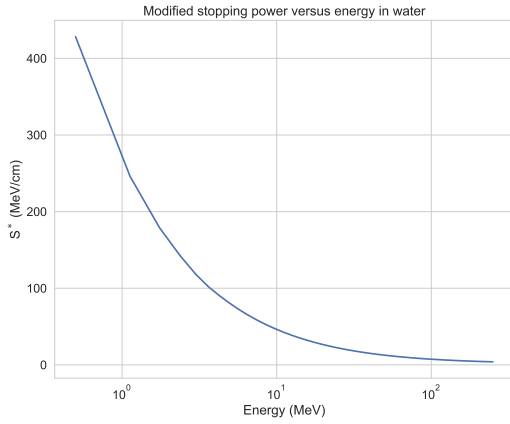


Figure 2: Water stopping power versus energy

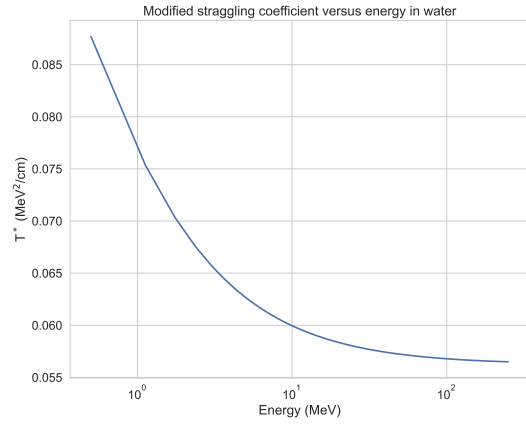


Figure 3: Water straggling coefficient versus energy

The straggling coefficient represents the statistical variation around the mean of the energy loss of a proton in a material. The consequence of energy straggling is the spreading of the energy spectrum of an initially mono-energetic beam [41]. The equation that was used for the straggling coefficient is [42]

$$T(E, N_{\mathbb{A}}) = \sum_{i \in \mathbb{A}} \frac{1}{(4\pi\epsilon_0)^2} N_i 4\pi e^4 Z_i \left( 1 + \frac{4I_i}{3m_e v_p^2} \ln \frac{2m_e v_p^2}{I_i} \right), \quad (29)$$

where  $N_{\mathbb{A}}$  is the set of atomic densities corresponding to the set of atoms  $\mathbb{A}$  that were considered to constitute human tissue, namely  $\mathbb{A} = \{\text{H, C, N, O, Na, Mg, P, S, Cl, Ar, K, Ca}\}$ . Moreover,  $Z_i$  is the atomic number of the target atom  $i$  with  $i \in \mathbb{A}$ ,  $\epsilon_0$  is the vacuum permittivity constant,  $e$  is the elementary charge,  $m_e$  is the electron mass,  $v_p$  is the proton speed,  $I_i$  is the mean atomic excitation energy of atom  $i$ . The straggling coefficient for protons versus energy in water can be seen in Figure 3.

The elastic scatter cross section can be found by considering the deflection that a proton suffers due to the Coulomb field of the nucleus. A derivation of this can be found in the work of Goldstein [43] who gives the microscopic elastic scatter cross section for protons incident on a target nucleus  $t, t \in \mathbb{A}$  with atomic number  $Z_t$  and atomic mass numbers  $A_t$  as

$$\sigma_{s,t}(E, \mu) = \frac{\left(1 + \frac{2\mu}{A_t} + \frac{1}{A_t^2}\right)^{3/2}}{1 + \frac{\mu}{A_t}} \left(\frac{Z_t e^2}{4\pi\epsilon_0 m_0 v_p^2}\right)^2 \frac{1}{(1 - \mu + 2\eta)^2}, \quad (30)$$

where  $m_0$  is the reduced mass which is defined by

$$\frac{1}{m_0} = \frac{1}{m_p} + \frac{1}{m_t}$$

with  $m_p$  the mass of the proton and  $m_t$  the mass of the target nucleus,  $v_p$  is the incident speed of the proton,  $\epsilon_0$  is the vacuum permittivity,  $e$  is the elementary charge and

$$\eta = \Theta_{min}^2 = \left( \frac{Z_t^{1/3} \alpha m_e c}{p} \right)^2$$

with  $m_e$  the electron mass,  $\alpha$  the fine structure constant,  $c$  the speed of light and  $p$  the momentum of the incident proton. Equation 30 is used to define the macroscopic scatter cross section as

$$\Sigma_s(E, \mu, N_{\mathbb{A}}) = \sum_{i \in \mathbb{A}} N_i \sigma_{s,i}(E, \mu) \quad (31)$$

with  $N_i, i \in \mathbb{A}$  the individual atomic density in the material under consideration.

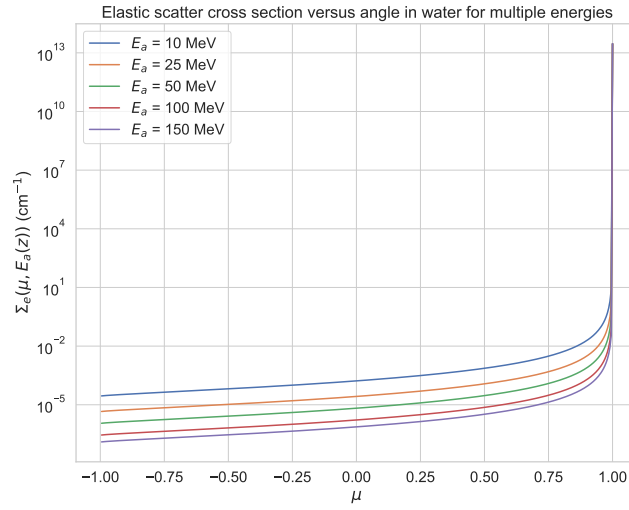


Figure 4: Water elastic scatter cross section for protons versus angle for multiple energies

## 5 Response change

Using the Fokker-Planck flux  $\varphi_{FP}$ , the FE coefficients from Equation 23 and a given set of system parameters  $\alpha$  the deposited energy in an arbitrary ROI is computed via

$$R(\alpha, \varphi_{FP}) = - \int_{ROI} dV \int_{4\pi} d\hat{\Omega} \int_{E_{min}}^{E_{max}} dE \left[ E \frac{\partial S\varphi}{\partial E} + E \frac{\partial}{\partial E} \left( T \frac{\partial \varphi}{\partial E} \right) - E \Sigma_a \varphi \right].$$

It is of interest to assess how the response changes depending on changes in the system parameters  $\alpha$ . This change in the response can be described as a direct and an indirect change. The direct change is the one that results from the change in the system parameters being directly used to compute the response. The indirect change comes through the FP flux and FE coefficients which are perturbed when changes in the system parameters are present. Thus, for each new vector of system parameters  $\alpha$  a new solution to the Fokker-Planck and Fermi-Eyges systems must be obtained.

This section describes the functional relationship between the change in the response  $\delta R$  and the changes in the system parameters  $\delta\alpha$  and the FP flux  $\delta\varphi_{FP}$ . Moreover, it describes a methodology that allows cheaply evaluating the desired change in the response without re-computing the Fokker-Planck flux and the Fermi-Eyges coefficients.

### 5.1 The change in the response

The response can be written using the ansatz from Equation 5 as

$$R(\alpha, \varphi_{FP}) = - \int_{ROI} dV \int_{4\pi} d\hat{\Omega} \varphi_{FE} \int_{E_{min}}^{E_{max}} dE \left[ E \frac{\partial S\varphi_{FP}}{\partial E} + E \frac{\partial}{\partial E} \left( T \frac{\partial \varphi_{FP}}{\partial E} \right) - E \Sigma_a \varphi_{FP} \right]. \quad (32)$$

Making use of the definition from Equation 28 for the  $4\pi$  integrated Fermi-Eyges flux allows writing the response from Equation 32 in a shortened form

$$R(\alpha, \varphi_{FP}) = \int_{ROI} dV \Psi_{FE}(\mathbf{r}) D_{FP}(z, \varphi_{FP}, \alpha), \quad (33)$$

where

$$D_{FP}(z, \varphi_{FP}, \alpha) = \left[ ES\varphi_{FP} \right]_{E_{min}} + \int_{E_{min}}^{E_{max}} dE S\varphi_{FP} + \int_{E_{min}}^{E_{max}} dE T \frac{\partial \varphi_{FP}}{\partial E} + \sum_{\Gamma_i} -[\varphi]T + \int_{E_{min}}^{E_{max}} dE E \Sigma_a \varphi_{FP}.$$

The change in the response due to changes in the system parameters can be found by computing the Gateaux-differential. Let  $\mathbf{e}^0 = (\alpha, \varphi_{FP})$  and  $\mathbf{h} = (\delta\alpha, \delta\varphi_{FP})$ . Then,

$$\delta R(\mathbf{e}^0, \mathbf{h}) = \frac{d}{dt} R(\mathbf{e}^0 + t\mathbf{h}) \Big|_{t=0} = \int_{ROI} dV [\delta \Psi_{FE}(\mathbf{r}) D_{FP}(z) + \Psi_{FE}(\mathbf{r}) \delta D_{FP}(z)]. \quad (34)$$

The Gateaux-differential of  $D_{FP}$  is computed to be

$$\begin{aligned} \delta D_{FP} &= \left\{ E \delta S \varphi_{FP} \Big|_{E_{min}} + \int_{E_{min}}^{E_{max}} dE \delta S \varphi_{FP} + \int_{E_{min}}^{E_{max}} dE \delta T \frac{\partial \varphi_{FP}}{\partial E} + \sum_{\Gamma_i} -[\varphi] \delta T + \int_{E_{min}}^{E_{max}} dE E \delta \Sigma_a \varphi_{FP} \right\} \\ &+ \left\{ ES \delta \varphi_{FP} \Big|_{E_{min}} + \int_{E_{min}}^{E_{max}} dE S \delta \varphi_{FP} + \int_{E_{min}}^{E_{max}} dE T \frac{\partial \delta \varphi_{FP}}{\partial E} + \sum_{\Gamma_i} -[\delta \varphi] T + \int_{E_{min}}^{E_{max}} dE E \Sigma_a \delta \varphi_{FP} \right\} \\ &= \delta D_{FP,dir}(\delta\alpha, \varphi_{FP}) + \delta D_{FP,indir}(\alpha, \delta\varphi_{FP}) \end{aligned}$$

where  $\delta D_{FP,dir}(\delta\boldsymbol{\alpha}, \varphi_{FP})$  is the direct change in the response due to the change in the system parameter vector and  $\delta D_{FP,indir}(\boldsymbol{\alpha}, \delta\varphi_{FP})$  is the indirect change in the response due to the perturbation in the dependent system variable.

The Gateaux-differential of  $\Psi_{FE}(\mathbf{r})$  is found to be

$$\delta\Psi_{FE}(\mathbf{r}) = \left. \frac{d}{dt} \Psi_{FE}(A + t\delta A, \bar{\xi}^2(z) + t\delta\bar{\xi}^2(z)) \right|_{t=0} = \Psi_{FE} \left[ \frac{2\delta A}{A} - \frac{\delta\bar{\xi}^2(z)}{\bar{\xi}^2(z)} + \frac{x^2 + y^2}{2} \frac{\delta\bar{\xi}^2(z)}{\bar{\xi}^2(z)^2} \right]. \quad (35)$$

The quantity  $\delta\Psi_{FE}(\mathbf{r})$  is thereafter laterally integrated over the X and Y extents of the ROI, namely

$$\begin{aligned} \iint_{ROI_{XY}} dx dy \delta\Psi_{FE} &= \iint_{ROI_{XY}} dx dy \Psi_{FE} \left[ \frac{2\delta A}{A} - \frac{\delta\bar{\xi}^2(z)}{\bar{\xi}^2(z)} + \frac{x^2 + y^2}{2} \frac{\delta\bar{\xi}^2(z)}{\bar{\xi}^2(z)^2} \right] \\ &= \left[ \frac{2\delta A}{A} - \frac{\delta\bar{\xi}^2(z)}{\bar{\xi}^2(z)} \right] \underbrace{\iint_{ROI_{XY}} dx dy \Psi_{FE}}_{I_{f1}} + \frac{\delta\bar{\xi}^2(z)}{\bar{\xi}^2(z)^2} \underbrace{\iint_{ROI_{XY}} dx dy \frac{x^2 + y^2}{2} \Psi_{FE}}_{I_{f2}} \\ &= \left[ \frac{2\delta A}{A} - \frac{\delta\bar{\xi}^2(z)}{\bar{\xi}^2(z)} \right] I_{f,1}(z) + \frac{\delta\bar{\xi}^2(z)}{\bar{\xi}^2(z)^2} I_{f,2}(z). \end{aligned} \quad (36)$$

At this point the term  $\delta A$  is set to zero. This term is only non-zero when the Fermi-Eyges initial condition is perturbed. For the purpose of this work, no such perturbation was included. Thus, the laterally integrated  $\delta\Psi_{FE}$  is given as

$$\iint_{ROI_{XY}} dx dy \delta\Psi_{FE} = \delta\bar{\xi}^2(z) \left[ -\frac{I_{f,1}(z)}{\bar{\xi}^2(z)} + \frac{I_{f,2}(z)}{\bar{\xi}^2(z)^2} \right]. \quad (37)$$

The term  $\delta\bar{\xi}^2(z)$  contains the unknown  $\delta\varphi_{FP}$ . Continuing the Gateaux-differential process results in

$$\delta\bar{\xi}^2(z) = \int_0^z (z - z')^2 \delta\Sigma_{tr}(z') dz' \text{ where } \delta\Sigma_{tr}(z) = \int_{-1}^1 \delta\Sigma_s(E_a(z), \mu) (1 - \mu) d\mu. \quad (38)$$

As the system parameters change, so does the Fokker-Planck flux  $\varphi_{FP}$ . This in turn results in a change in the average depth-dependent energy  $E_a(z)$  of the beam which in turn results ultimately in changes in the FE coefficients. To compute the effect of a change in the FP flux on the FE coefficients, the elastic scatter cross section can be re-written to illustrate the energy dependence by using the classical kinetic energy relationship between speed and energy as

$$\begin{aligned} \Sigma_s(E_a(z), \mu, N_{\mathbb{A}}) &= \sum_{i \in \mathbb{A}} N_i F_1(\mu, A_i) F_2(Z_i, m_{0i}) \frac{1}{E_a^2} \frac{1}{\left(1 - \mu + \frac{2c_{\eta,i}}{E_a}\right)^2}, \\ \text{where } F_1(\mu, A_i) &= \frac{\left(1 + \frac{2\mu}{A_i} + \frac{1}{A_i^2}\right)^{3/2}}{1 + \frac{\mu}{A_i}}, \quad F_2(Z_i, m_{0i}) = \left(\frac{Z_i e^2 m_p}{8\pi\epsilon_0 m_{0i}}\right)^2 \text{ and } c_{\eta,i} = E_a \eta_i. \end{aligned}$$

The Gateaux-differential of the elastic scatter cross section is

$$\begin{aligned} \delta\Sigma_s(E_a(z), \mu, N_{\mathbb{A}}) &= \left. \frac{d}{dt} \sum_{i \in \mathbb{A}} (N_i + t\delta N_i) F_1(\mu, A_i) F_2(Z_i, m_{0i}) \frac{1}{(E_a(z) + t\delta E_a(z))^2} \frac{1}{\left(1 - \mu + \frac{2c_{\eta,i}}{E_a(z) + t\delta E_a(z)}\right)^2} \right|_{t=0} \\ &= \sum_{i \in \mathbb{A}} \delta N_i F_1(\mu, A_i) F_2(Z_i, m_{0i}) \frac{1}{E_a(z)^2} \frac{1}{\left(1 - \mu + \frac{2c_{\eta,i}}{E_a(z)}\right)^2} \\ &\quad + \sum_{i \in \mathbb{A}} N_i F_1(\mu, A_i) F_2(Z_i, m_{0i}) \frac{\delta E_a(z)}{E_a(z)^2} \frac{1}{\left(1 - \mu + \frac{2c_{\eta,i}}{E_a(z)}\right)^2} \left[ \frac{-2}{E_a(z)} + \frac{4c_{\eta,i}}{E_a^2(z)} \frac{1}{1 - \mu + \frac{2c_{\eta,i}}{E_a(z)}} \right] \\ &= \delta\Sigma_{s1}(\delta N_{\mathbb{A}}) + \delta\Sigma_{s2}(\delta E_a(z)), \end{aligned} \quad (39)$$

where  $\delta N_{\mathbb{A}}$  is the set of perturbations in the atomic density set previously defined as  $N_{\mathbb{A}}$ . It can be seen that here as well the change in the elastic scatter cross section can be described as a direct change due to the atomic composition in the tissue  $\delta N_{\mathbb{A}}$  and the change due to the change in the beam energy spectrum. The last component is to obtain the relationship between the change in the energy spectrum  $\delta E_a(z)$  and the change in the flux itself  $\delta \varphi_{FP}$ . The Gateaux-differential of the average depth-dependent energy is

$$\delta E_a(z) = \frac{1}{N_p(z)} \int_0^\infty dE E \delta \varphi_{FP} - \frac{E_b(z)}{N_p(z)^2} \int_0^\infty dE \delta \varphi_{FP}, \quad (40)$$

where the number of particles and the beam energy at a given depth are defined as

$$N_p(z) = \int_0^\infty dE \varphi_{FP}(z, E) \text{ and} \quad (41)$$

$$E_b(z) = \int_0^\infty dE E \varphi_{FP}(z, E). \quad (42)$$

At this point the functional relationship between  $\delta R$  and the changes in  $\delta \alpha$  and  $\delta \varphi_{FP}$  can be obtained. The first step is to introduce the result from Equation 39 into the Gateaux-differential of  $\bar{\xi}^2$  given in Equation 38, yielding

$$\begin{aligned} \delta \bar{\xi}^2(z) &= \int_0^z dz' (z - z')^2 \delta \sigma_{tr}(z') = \int_0^z dz' (z - z')^2 \int_{-1}^1 d\mu [\delta \Sigma_{s1}(\delta N_{\mathbb{A}}) + \delta \Sigma_{s2}(\delta E_a(z))](1 - \mu) \\ &= \delta \bar{\xi}^2_1(\delta N_{\mathbb{A}}) + \delta \bar{\xi}^2_2(\delta E_a(z)). \end{aligned} \quad (43)$$

The term  $\delta \bar{\xi}^2_1$  does not contain any dependencies on the unknown  $\delta \varphi_{FP}$  and contributes to the direct effect. The term  $\delta \bar{\xi}^2_2$  does on the other hand contain a dependency on  $\delta \varphi_{FP}$ . Its  $\delta \varphi_{FP}$  dependency is obtained by using Equation 40, namely

$$\begin{aligned} \delta \bar{\xi}^2_2 &= \int_0^z dz' (z - z')^2 \\ &\quad \underbrace{\int_{-1}^1 d\mu (1 - \mu) \sum_{i \in \mathbb{A}} N_i F_1(\mu, A_i) F_2(Z_i, m_{0i}) \frac{\delta E_a(z')}{E_a(z')^2} \frac{1}{\left(1 - \mu + \frac{2c_{\eta,i}}{E_a(z')}\right)^2} \left[ \frac{-2}{E_a(z')} + \frac{4c_{\eta,i}}{E_a^2(z')} \frac{1}{1 - \mu + \frac{2c_{\eta,i}}{E_a(z')}} \right]}_{\delta E_a(z') \cdot I_\mu(z')} \\ &= \int_0^z dz' (z - z')^2 \delta E_a(z') I_\mu(z') = \int_0^z dz' (z - z')^2 I_\mu(z') \int_0^\infty dE \left( \frac{E}{N_p(z')} - \frac{E_b(z')}{N_p(z')^2} \right) \delta \varphi_{FP}(z', E). \end{aligned}$$

The next step is to introduce the expression from Equation 43 into the lateral ROI integration of  $\delta \Psi_{FE}$  from Equation 37. For simplicity of notation, let

$$\Psi_{FE}^{ROI_{xy}}(z) = \int_{ROI_{xy}(z)} dx dy \Psi_{FE}.$$

Using this,  $\delta R$  becomes

$$\delta R = \int_{ROI_z} dz D_{FP}(z) \int_{ROI_{xy}} dx dy \delta \Psi_{FE} + \int_{ROI_z} dz \Psi_{FE}^{ROI_{xy}}(z) \delta D_{FP}(z). \quad (44)$$

Introducing in this expression the direct and indirect contributions results in

$$\begin{aligned}
\delta R &= \int_{ROI_z} dz \left\{ D_{FP}(z) \delta \bar{\xi}^2(z) \left[ -\frac{I_{f,1}(z)}{\xi^2(z)} + \frac{I_{f,2}(z)}{\xi^2(z)^2} \right] \right\} + \int_{ROI_z} dz \Psi_{FE}^{ROI_{xy}}(z) [\delta D_{FP,dir}(\delta \alpha) + \delta D_{FP,indir}(\delta \varphi_{FP})] \\
&= \int_{ROI_z} dz D_{FP}(z) \delta \bar{\xi}^2_1(\delta N_{\mathbb{A}}) \left[ -\frac{I_{f,1}(z)}{\xi^2(z)} + \frac{I_{f,2}(z)}{\xi^2(z)^2} \right] \rightarrow \text{direct change due to } \delta \alpha \\
&+ \int_{ROI_z} dz D_{FP}(z) \delta \bar{\xi}^2_2(\delta \varphi_{FP}) \left[ -\frac{I_{f,1}(z)}{\xi^2(z)} + \frac{I_{f,2}(z)}{\xi^2(z)^2} \right] \rightarrow \text{indirect change due to } \delta \varphi_{FP} \\
&+ \int_{ROI} dz \Psi_{FE}^{ROI_{xy}}(z) \delta D_{FP,dir}(\delta \alpha, \varphi_{FP}) \rightarrow \text{direct change due to } \delta \alpha \\
&+ \int_{ROI} dz \Psi_{FE}^{ROI}(z) \delta D_{FP,indir}(\alpha, \delta \varphi_{FP}) \rightarrow \text{indirect change due to } \delta \varphi_{FP}. \tag{45}
\end{aligned}$$

## 5.2 Relating $\delta \varphi$ to $\delta \alpha$

The expression in Equation 45 shows that the response change depends on the changes in the system parameter vector  $\delta \alpha$  and the corresponding change in the Fokker-Planck flux  $\delta \varphi_{FP}$ . Since the Fokker-Planck flux and the vector of system parameters are related through Equation 10 and its associated boundary conditions it must also be that the perturbations in both of these quantities are related. A first-order relationship between  $\delta \varphi_{FP}$  and  $\delta \alpha$  can be obtained by taking the Gateaux-differential of the Fokker-Planck equation and it's boundary conditions [29]. In this process a new PDE is obtained for the unknown  $\delta \varphi_{FP}$  as a function of the initial operator  $L(\alpha)$  and the perturbations in the system parameters  $\delta \alpha$ . Given that this PDE has to be solved for each new vector of system parameter perturbations and the number of such vectors is large, this process is computationally too expensive to implement in practice.

## 5.3 Adjoint sensitivity analysis procedure

An alternative to the procedure from subsection 5.2 is the Adjoint Sensitivity Analysis Procedure (ASAP). ASAP aims to eliminate the unknown value of  $\delta \varphi_{FP}$  from the response change Equation 45. This is done by constructing a new system called the adjoint system that is independent of  $\delta \varphi_{FP}$  with the property that the solution of this system (denoted by  $\varphi^\dagger$ ) can be used to eliminate the unknown  $\delta \varphi_{FP}$  from Equation 45. In the process of constructing the adjoint system the boundary conditions that ensure its unique solution will also have to be imposed. These must be chosen such that [29]:

- they are independent of  $\delta \varphi_{FP}$ ,  $\delta \alpha$  and Gateaux-derivatives with respect to  $\alpha$ , and
- the evaluation of boundary terms does not contain unknown values of  $\delta \varphi_{FP}$ .

## 5.4 Adjoint system derivation

The starting point of the adjoint system derivation is the inner product between the adjoint flux and the operator acting on the perturbation  $\delta \varphi_{FP}$ , namely

$$\langle \varphi^\dagger, L(\alpha) \delta \varphi_{FP} \rangle = \int_0^\infty dz \int_0^\infty dE \varphi^\dagger \left[ \frac{\partial \delta \varphi_{FP}}{\partial z} - \frac{\partial S \delta \varphi_{FP}}{\partial E} - \frac{\partial}{\partial E} \left( T \frac{\partial \delta \varphi_{FP}}{\partial E} \right) + \Sigma_a \delta \varphi_{FP} \right] \tag{46}$$

At this point we extend  $\varphi_{FP}$  and consequently  $\delta \varphi_{FP}$  to the whole  $\mathbb{R}^2$  plane with the condition that these quantities are zero everywhere outside of the computational domain  $\mathcal{D}$ . Through partial integration,



Equation 46 is found to be equal to

$$\begin{aligned}\langle \varphi^\dagger, L(\boldsymbol{\alpha}) \delta\varphi_{FP} \rangle &= \int_0^\infty dE \varphi^\dagger(0, E) \delta\varphi_{FP}(0, E) + \left\langle -\frac{\partial \varphi^\dagger}{\partial z} + S \frac{\partial \varphi^\dagger}{\partial E} - \frac{\partial}{\partial E} T \frac{\partial \varphi^\dagger}{\partial E} + \Sigma_a \varphi^\dagger, \delta\varphi_{FP} \right\rangle \\ &= \int_0^\infty dE \varphi^\dagger(0, E) \delta\varphi_{FP}(0, E) + \langle L^\dagger(\alpha^0) \varphi^\dagger, \delta\varphi_{FP} \rangle.\end{aligned}\quad (47)$$

In the process of deriving Equation 47 the adjoint operator  $L^\dagger$  together with its associated boundary conditions were found to be

$$L^\dagger \varphi^\dagger = -\frac{\partial \varphi^\dagger}{\partial z} + S \frac{\partial \varphi^\dagger}{\partial E} - \frac{\partial}{\partial E} \left( T \frac{\partial \varphi^\dagger}{\partial E} \right) + \Sigma_a \varphi^\dagger \quad (48)$$

$$\text{BCE: } \varphi^\dagger(z, E_{min}) = 0, \quad \frac{\partial \varphi^\dagger}{\partial E} \Big|_{E=E_{min}} = 0, \quad (49)$$

$$\text{BCS: } \varphi^\dagger(z_{max}, E) = 0. \quad (50)$$

To achieve the desired  $\delta\varphi_{FP}$  elimination from Equation 45 we note that  $\delta R$  is linear in both  $\delta\boldsymbol{\alpha}$  and  $\delta\varphi_{FP}$ . This allows writing the Gateaux-differential of the response as [29]

$$\delta R(\mathbf{e}^0; \mathbf{h}) = R'_\varphi(\mathbf{e}^0) \delta\varphi_{FP} + R'_\alpha(\mathbf{e}^0) \delta\boldsymbol{\alpha}. \quad (51)$$

The quantity denoted as  $R'_\varphi(\mathbf{e}^0) \delta\varphi_{FP}$ , identified as

$$R'_\varphi(\mathbf{e}^0) \delta\varphi_{FP} = \int_{ROI_z} dz D_{FP}(z) \delta \bar{\xi}^2_2(\delta\varphi_{FP}) \left[ -\frac{I_{f,1}(z)}{\xi^2(z)} + \frac{I_{f,2}(z)}{\xi^2(z)^2} \right] + \int_{ROI} dz \Psi_{FE}^{ROI_{xy}}(z) \delta D_{FP,indir}(\delta\varphi_{FP}),$$

is itself also linear in  $\delta\varphi_{FP}$ . Coupling this with the self-duality of Hilbert spaces certifies the application of Riesz's representation theorem. Using this theorem the quantity  $R'_\varphi(\mathbf{e}^0) \delta\varphi_{FP}$  can be written as an inner product between a quantity  $r^\dagger \in \mathcal{H}$  and  $\delta\varphi_{FP}$ , namely [29],

$$R'_\varphi(\mathbf{e}^0) \delta\varphi_{FP} = \langle r^\dagger, \delta\varphi_{FP} \rangle. \quad (52)$$

Identifying  $r^\dagger$  as the right-hand side of the adjoint system allows writing the Gateaux-differential of the response as

$$\delta R(\mathbf{e}^0; \mathbf{h}) = \langle r^\dagger, \delta\varphi_{FP} \rangle + R'_\alpha(\mathbf{e}^0) \delta\boldsymbol{\alpha} = \langle L^\dagger(\boldsymbol{\alpha}) \varphi^\dagger, \delta\varphi_{FP} \rangle + R'_\alpha(\mathbf{e}^0) \delta\boldsymbol{\alpha}. \quad (53)$$

The inner product in the second equality has already been computed in Equation 47. Thus,

$$\delta R(\mathbf{e}^0; \mathbf{h}) = \langle \varphi^\dagger, L(\boldsymbol{\alpha}) \delta\varphi_{FP} \rangle - \int_0^\infty dE \varphi^\dagger(0, E) \delta\varphi_{FP}(0, E) + R'_\alpha(\mathbf{e}^0) \delta\boldsymbol{\alpha}. \quad (54)$$

The quantity  $L(\boldsymbol{\alpha}) \delta\varphi_{FP}$  can be derived by taking the Gateaux-differential of the Fokker-Planck equation, and is found to be

$$L(\boldsymbol{\alpha}) \delta\varphi_{FP} = -[L'_\alpha(\boldsymbol{\alpha}) \varphi_{FP}] \delta\boldsymbol{\alpha} = \frac{\partial \delta S \varphi_{FP}}{\partial E} + \frac{\partial}{\partial E} \left( \delta T \frac{\partial \varphi_{FP}}{\partial E} \right) - \delta \Sigma_a \varphi_{FP}. \quad (55)$$

Making use of this transforms  $\delta R(\mathbf{e}^0; \mathbf{h})$  to

$$\delta R(\mathbf{e}^0; \mathbf{h}) = \langle \varphi^\dagger, -[L'_\alpha(\boldsymbol{\alpha}) \varphi_{FP}] \delta\boldsymbol{\alpha} \rangle - \int_0^\infty dE \varphi^\dagger(0, E) \delta\varphi(0, E) + R'_\alpha(\mathbf{e}^0) \delta\boldsymbol{\alpha}, \quad (56)$$

where the first inner product is equal to

$$\langle \varphi^\dagger, -[L'_\alpha(\alpha)\varphi_{FP}] \delta\alpha \rangle = \int_0^\infty dz \int_0^\infty dE \varphi^\dagger \left[ \frac{\partial}{\partial E} \delta S \varphi_{FP} + \frac{\partial}{\partial E} \delta T \frac{\partial \varphi_{FP}}{\partial E} - \delta \Sigma_a \varphi_{FP} \right]. \quad (57)$$

For simplicity, the quantity  $\delta\varphi(0, E)$  was set to zero in the case of this work and  $R'_\alpha(\mathbf{e}^0) \delta\alpha$  is the direct change that has been previously computed in Equation 45 as

$$R'_\alpha(\mathbf{e}^0) \delta\alpha = \int_{ROI_z} dz D_{FP}(z) \delta \bar{\xi}^2_1 (\delta N_i) \left[ -\frac{I_{f,1}(z)}{\bar{\xi}^2(z)} + \frac{I_{f,2}(z)}{\bar{\xi}^2(z)^2} \right] + \int_{ROI_z} dz \Psi_{FE}^{ROI}(z) \delta D_{FP,dir}(\delta\alpha). \quad (58)$$

As can be seen from Equations (56) to (58) the goal of the ASAP has been reached. The indirect change in the response due to the perturbation of the Fokker-Planck flux  $\delta\varphi_{FP}$  has been replaced in Equation 45 by the inner product from Equation 57. Thus, for a given number  $N$  of different vectors of system parameters  $\alpha$  the computational expense has been decreased from the initial  $N$  necessary solutions of the 1DFP system to just two solutions, namely those of the adjoint and Fokker-Planck systems, with a similar computational expense for both systems.

## 6 Results and discussion

This section details the computational set-up of the algorithm in Subsection 6.1, the comparison between the dose calculation of our engine and those of TOPAS and Bortfeld's method in Subsection 6.2 and the accuracy of the previously illustrated ASAP methodology for response change computations in Subsection 6.3.

### 6.1 Computational set-up

The domain of the CT scan was discretized using an arbitrarily chosen number of 51 bins in the X and Y direction and 100 bins in the Z direction. The spatial extent of the CT scan was set to -2 to 2 cm in the X and Y directions and 0 to 10 cm in the Z direction. Within this geometry a slab was placed along the depth of the tank with its depth and precise position being variable. The slab had variable HU values set while the rest of the tank was set to either 0 HU (water) or the arbitrarily chosen value of 550 HU. The ROI was defined to be a box with variable extents in all three directions. An illustration of this set-up can be seen in Figure 5

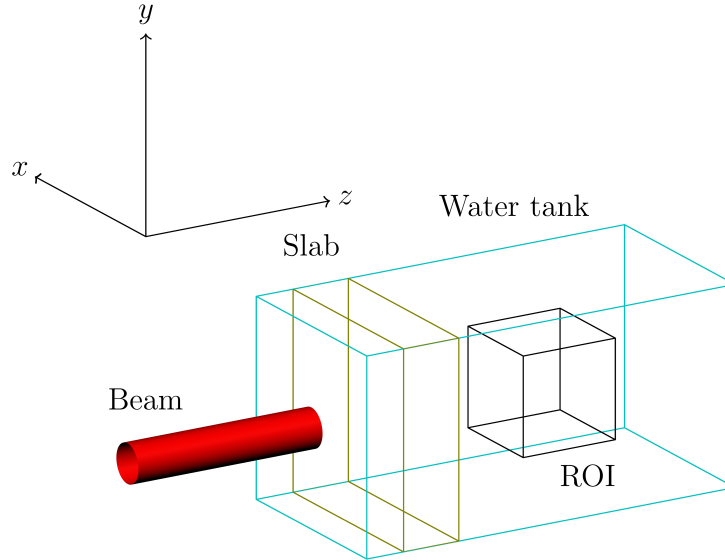


Figure 5: Illustration of the CT scan, the slab with perturbed HU values, the ROI and the incident beam

In all test cases the beam started at the point of  $\mathbf{r}_{start} = (0, 0, 0)$  and ended at  $\mathbf{r}_{end} = (0, 0, 10)$ . The tracking of the beam within the geometry was performed using an in-house ray-tracing procedure based on work of de Sutter et al. [44]. A von Neumann stability analysis was not performed however, through empirical observations it was found that in water the maximal step size for accurate, artifact free fluxes outputted by the CN scheme is 0.01 cm. This was used in a wrapper function for the ray-tracing procedure to divide each segment into a corresponding number of sub-segments.

The initial spread of the Gaussian  $\sigma_\xi$  from Equation 25 in X and Y was set to 0.3 cm and the space angle correlation  $\rho$  from Equation 25 was set to zero. Due to the singularity in the angular spread variable of the coefficients from Equation 25,  $\sigma_\omega$  could not be set to zero. However, it was found that values below  $10^{-4}$  did not affect the resulting energy deposition distributions and thus the angular spread was set to the dimensionless value of  $10^{-8}$ . The energy domain was fixed between  $E_{min} = 1$  MeV,  $E_{max} = 100$  MeV with a number of groups of  $NG = 300$ . The coefficients of the energy initial condition from Equation 11 were set to correspond to a normal distribution and were matched such that the number of particles was either 1 or  $2 \times 10^7$ . Moreover, the initial beam average energy  $E_0$  from Equation 12 was set to 100 MeV while the energy spread  $\sigma_E$  from the same equation was set to 0.757 504 MeV. The energy spread value was chosen to match the standard value that TOPAS initializes for a proton pencil beam.

## 6.2 Forward results

To gauge the accuracy of the reponse computation engine, it was benchmarked against the TOPAS MC algorithm [39]. In a homogeneous water tank the energy deposition can readily be converted to dose deposition. Laterally integrating this three dimensional quantity results in the dose-depth curve named integrated depth dose (IDD). The comparison against TOPAS and Bortfeld’s popular pencil beam algorithm [45] can be seen in Figure 6 showing that our algorithm is capable of accurately predicting the dose in the Bragg peak, the region of most clinical interest. Our algorithm slightly over-estimates the dose in the entrance region, due to the assumption that 100 % of the energy released in nuclear interactions is deposited locally. A refinement of the treatment of nuclear interactions can be envisioned using convolutional methods or through more simplistic fits to empirical data. However, this is not the purpose of this paper, whose main focus is the sensitivity of the algorithm.

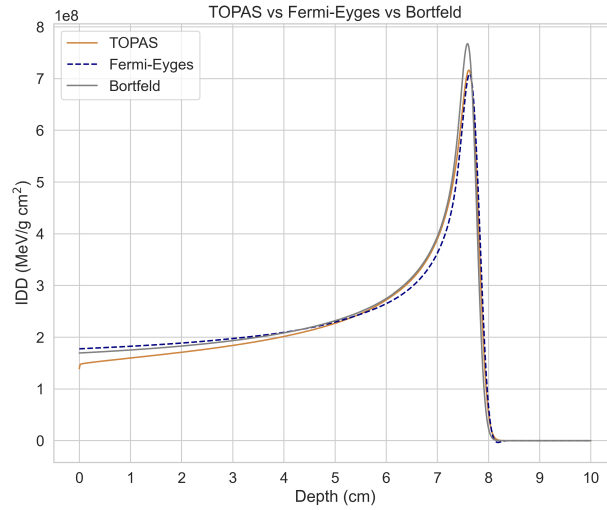


Figure 6: IDD of the in-house algorithm, TOPAS and Bortfeld’s model

## 6.3 Adjoint results

Case number	Slab		ROI extent			Maximal percentage error
	Location (cm)	Perturbation (HU)	X (cm)	Y (cm)	Z (cm)	
I	[2, 3]	[-40, 40]	[-2, 2]	[-2, 2]	[0, 2]	0
II	[2, 3]	[-40, 40]	[-2, 2]	[-2, 2]	[2, 6.5]	$1.1 \times 10^{-6}$
III	[2, 3]	[-40, 40]	[-2, 2]	[-2, 2]	[5, 6.5]	$3.6 \times 10^{-3}$
III	[2, 3]	[-40, 40]	[-0.3, 0.3]	[-0.3, 0.3]	[5, 6.5]	$3.6 \times 10^{-3}$
IV	[2, 3]	[-40, 40]	[-0.3, 0]	[-0.3, 0.3]	[5, 6.5]	$3.6 \times 10^{-3}$
V	[2, 3]	[-400, 400]	[-2, 2]	[-2, 2]	[7, 9]	3.0
V	[2, 3]	[-400, 400]	[-0.3, 0.3]	[-0.3, 0.3]	[7, 9]	3.0
VI	[4, 6]	[-40, 40]	[-2, 2]	[-2, 2]	[5, 6.5]	$3.6 \times 10^{-3}$
VI	[4, 6]	[-40, 40]	[-0.3, 0.3]	[-0.3, 0.3]	[5, 6.5]	$3.6 \times 10^{-3}$
VI	[4, 6]	[-400, 400]	[-2, 2]	[-2, 2]	[7, 9]	17.7
VI	[4, 6]	[-400, 400]	[-0.3, 0.3]	[-0.3, 0.3]	[7, 9]	17.7

Table 1: Overview of case numbers and the corresponding slab location and perturbation values, ROI values and maximal percentage errors between the re-computation and the adjoint result.

A variety of test cases for the response change computation was performed, an overview of which can be seen in Table 1. For all test cases  $\Sigma_a$  was set to zero due to a lack of data for all other materials other

than 0 HU.

### 6.3.1 Case I

First, a small range of  $[-40, 40]$  HU perturbations around the nominal slab value of 550 HU was used. The slab was placed in the plateau region of the energy deposition versus depth curve between 2 and 3 cm in depth. Given this set-up if the ROI has dimensions  $X, Y \in [-2, 2], Z \in [0, 2]$  and under the assumption of a forward propagating (not backscattered) flux then the expectation is that the response change is identically zero. This correctness test can be seen in Figure 7.

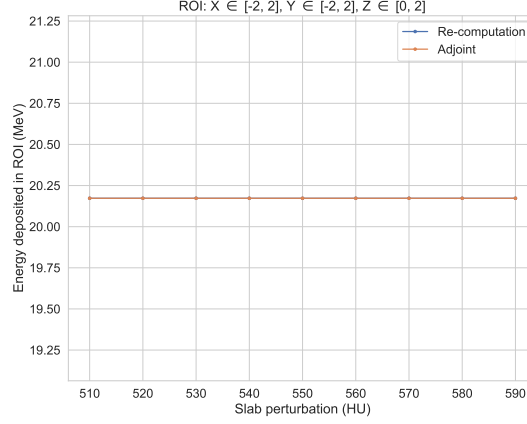


Figure 7: Adjoint versus re-computation for a small HU range with a full lateral ROI in X and Y and  $Z \in [0, 2]$ .

### 6.3.2 Case II

Changing the ROI to be the box with  $X, Y \in [-2, 2], Z \in [2, 6.5]$  results in Figure 8. There it can be seen that adjoint theory provides a first order approximation to the forward response. In this case the maximal percent error occurs for the 510 HU slab perturbation and it is equal to  $\approx 1.1 \times 10^{-6} \%$ .

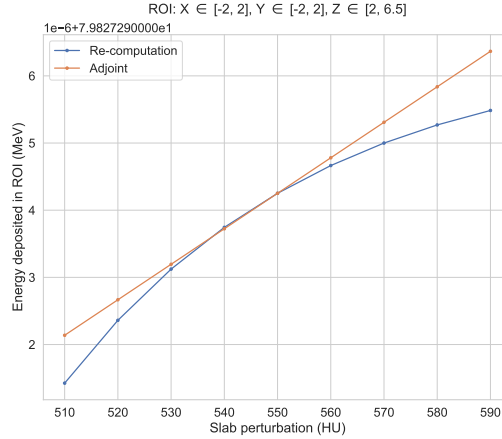


Figure 8: Adjoint versus re-computation for a small HU range with a full lateral ROI in X and Y,  $Z \in [2, 6.5]$ .

### 6.3.3 Case III

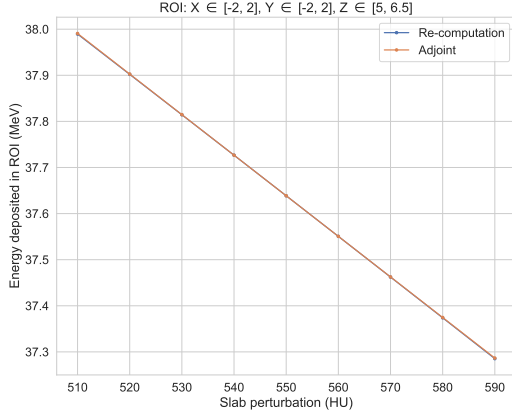


Figure 9: Adjoint versus re-computation for a small HU range with a full lateral ROI in X and Y and Z  $\in [5, 6.5]$ .

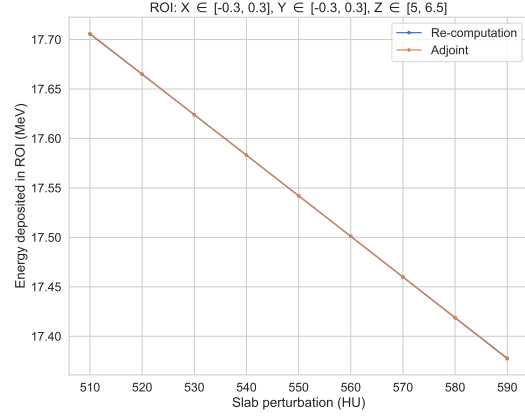


Figure 10: Adjoint versus re-computation for a small HU range with a reduced lateral ROI in X and Y and Z  $\in [5, 6.5]$ .

In the case of proton therapy, it is likely that a ROI of practical interest is the Bragg Peak region. Thus, the slab is maintained in its previous position and the ROI is set to the box with  $X, Y \in [-2, 2], Z \in [5, 6.5]$ . This result can be seen in Figure 9. Another scenario of interest could be the one in which a tumor is surrounded by organs at risk. In this case, the ROI is restricted to only part of the lateral extent. In Figure 10 the lateral extent was constrained to  $X, Y \in [-0.3, 0.3]$  while the depth was kept to  $Z \in [5, 6.5]$ . Both Figure 9 and 10 show that the adjoint method is capable of accurately computing the response changes due to the slab in the ROI down to a percentage error of  $3.6 \times 10^{-3} \%$  that is likely clinically insignificant. This can be seen from the fact that a fraction that is typically delivered is on the order of 2 Gy which is equivalent to  $\approx 6.3 \times 10^9 \text{ MeV g}^{-1}$ .

### 6.3.4 Case IV

Tests with asymmetric ROIs have also been performed. Restricting the ROI such that  $X \in [-0.3, 0], Y \in [-0.3, 0.3]$  and keeping  $Z \in [5, 6.5]$  resulted in a similar error (depicted as the same in Table 1 due to round-off) to the previous test cases. The two curves for this case can be seen in Figure 11.

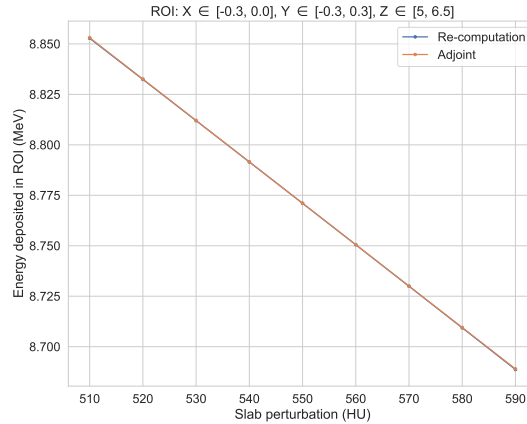


Figure 11: Adjoint versus re-computation for a small HU range with an laterally asymmetric ROI in X and Y and Z  $\in [5, 6.5]$ .

### 6.3.5 Case V

Next to the small HU range, a large  $[-400, 400]$  HU perturbation range around the nominal value of 0 HU was tested. The nominal value in this case corresponded to a homogeneous water tank. This set-up simulates more clinically relevant test-cases as the -400 HU value roughly corresponds to a tissue similar to lung while a value of 400 HU corresponds to bone. As in the small perturbation range cases, ROIs with full and reduced lateral X and Y extents were tested. Figure 13 illustrates the case when  $X \in [-2, 2]$ ,  $Y \in [-2, 2]$ ,  $Z \in [7, 9]$  while Figure 14 illustrates the case when  $X \in [-0.3, 0.3]$ ,  $Y \in [-0.3, 0.3]$ ,  $Z \in [7, 9]$ . It should be noted that as opposed to the straight lines shown before, these figures do not contain straight lines. This is due to the regions of discontinuity that appear in the Schneider's conversion [38] from HU values to density and atomic composition. The discontinuity for the density to HU conversion can be seen in Figure 12 and it is also why the range of 510 to 590 was chosen initially, as in this range the afore mentioned conversion is continuous.

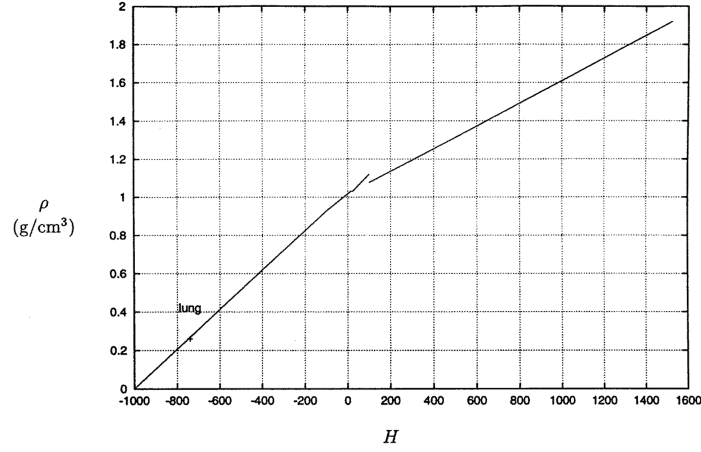


Figure 12: Illustration of the discontinuity in Schneider's HU to density conversion curve. Picture taken from [38]

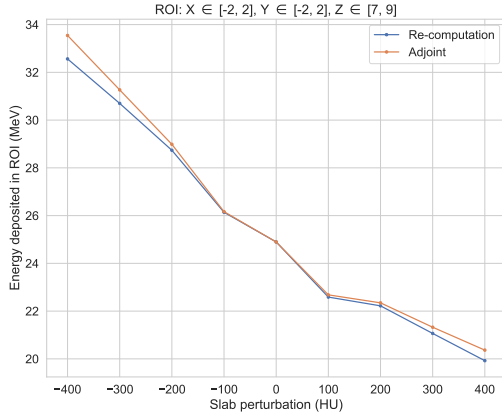


Figure 13: Adjoint versus re-computation for a large HU range with a laterally symmetric ROI and  $Z \in [7, 9]$ .

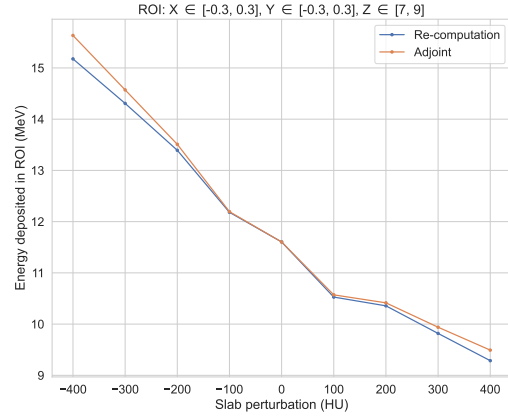


Figure 14: Adjoint versus re-computation for a large HU range with a laterally symmetric reduced ROI and  $Z \in [7, 9]$ .

### 6.3.6 Case VI

Tests were also performed with a 2 cm slab placed between 4 and 6 cm deep, in the vicinity of the BP. The same large and small variations in the perturbation range together with ROI contractions were investigated. In the case of a small perturbation range, good agreement was found for both full and symmetrically reduced lateral X and Y extents with maximal percentage errors being  $3.6 \times 10^{-3} \%$ . In the case of the large perturbation range, the algorithm resulted in a moderate percentage error of 17%. This result is not unexpected as adjoint theory provides a first order approximation to the response change and it is expected that the approximation worsens as a function of increasing perturbations.

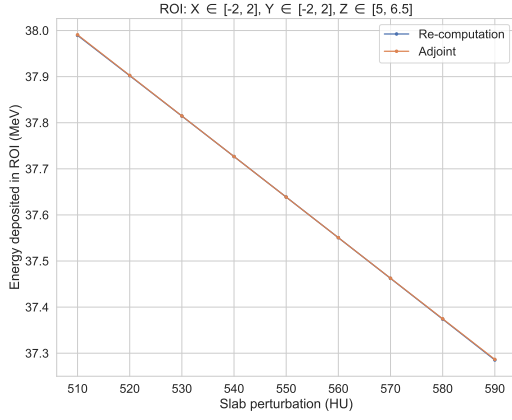


Figure 15: Adjoint versus re-computation for a small HU range with a laterally symmetric ROI and  $Z \in [5, 6.5]$ .

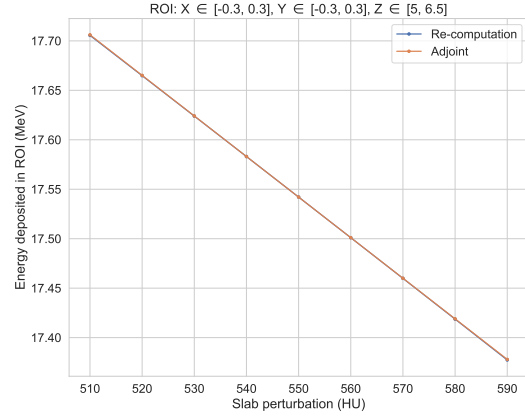


Figure 16: Adjoint versus re-computation for a large HU range with a laterally reduced symmetric ROI and  $Z \in [5, 6.5]$ .

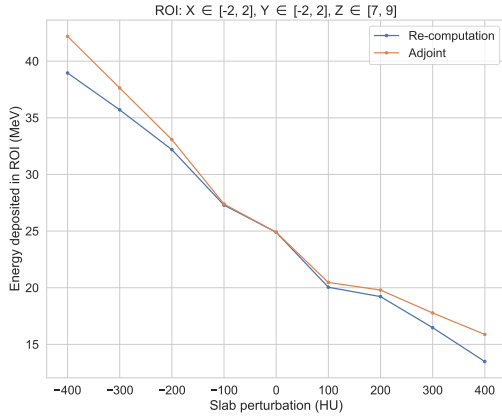


Figure 17: Adjoint versus re-computation for a large HU range with a laterally symmetric ROI and  $Z \in [7, 9]$ .

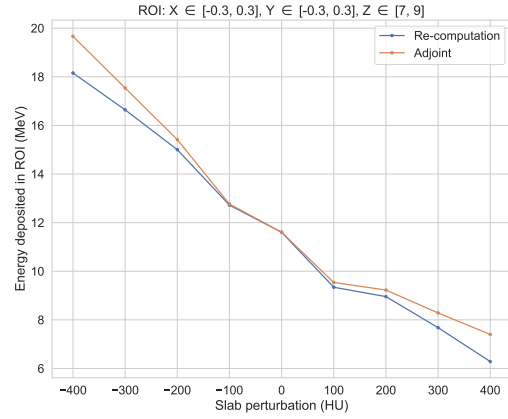


Figure 18: Adjoint versus re-computation for a large HU range with a laterally symmetrically reduced ROI and  $Z \in [7, 9]$ .



## 7 Conclusion

In this paper we have developed a methodology for the approximate solution of the Linear Boltzmann Equation that takes heterogeneity in the depth direction into account. This method requires the solution to two PDEs, namely the one-dimensional FP equation and the FE equation. The one-dimensional FP equation was numerically solved through a combination of the SIPG method using quadratic energy basis functions in energy and the CN method in space. Using the 1DFP flux  $\varphi_{FP}$  the average depth-dependent energy  $E_a(z)$  of the beam is computed. This quantity is thereafter used in the computation of the depth-dependent FE coefficients which define the FE flux  $\varphi_{FE}$ . Using the product of these two fluxes complete knowledge of the phase-space density of protons is obtained and hereby our specific problem of charged particle transport is solved.

Using the phase-space density of protons, the response (which was defined by the deposited energy in an arbitrary ROI) was computed. Good agreement, especially in the clinically significant Bragg peak region, was obtained in a homogeneous water tank when our algorithm was benchmarked against TOPAS (taken as the reference algorithm) and Bortfeld’s popular pencil beam algorithm.

Using functional analysis the adjoint system was derived and solved. The changes in the response due to slabs placed along the depth of the tank with different HU values were computed. These changes were compared against the re-computation ones with relatively good results. Adjoint theory provided (as expected) a first order approximation to the response change curve. In the case of small slab perturbations the relative difference was clinically insignificant. Even in cases of large HU perturbations, adjoint theory resulted in relatively small to moderate errors of 3 % to 17 %.

Future work should focus both on improving the energy/dose deposition component (forward) and on speeding up the response change computation (backward). To improve the forward component a better model is needed for the inelastic nuclear interactions between the primary protons and the irradiated tissue. Possible methods for approaching this would be a convolution-based approach or the Monte-Carlo fit method outlined by Soukup et al. [46]. Moreover, it is clear that our algorithm cannot in its current state account for lateral heterogeneities and thus, a pencil beam splitting scheme is needed. A starting point for this would be the well-performing scheme proposed by Yang et. al [47]. Another metric to improve on is speed. This is an area where our algorithm performed relatively well, with an average execution time of 0.1 s for one pencil beam. Ultimately, we aim to reduce the execution time down to the ms range. This can be achieved by implementing an adaptive energy grid such that no empty energy groups are solved for. Moreover, the process of tracking many beams through the CT scan is highly parallelizable due to their independent nature.

The main drawback of the adjoint component is the long time presently needed to compute the direct contribution to the response change due to  $\delta N_{\mathbb{A}}$  versus the relatively small increase in accuracy it yields. Tabulating the integrals involved should, similar to the forward component, yield significant time reductions. Moreover, the necessary data for the absorption cross section should be obtained. Another point of improvement is the inclusion of perturbations in the initial values of the FE coefficients or of the FP boundary condition coefficients. Such perturbations can be derived from machine log-files (for example the difference in MU values for a point is related to a difference in the number of input protons and the difference in the spot positions is related to a different entry position and angle of the beam) and are the way in which our algorithm can be used for the purpose of patient-specific quality assurance.

## 8 Conflicts of interest and acknowledgements

The authors wish to acknowledge that the manuscript is partly funded by Varian, a Siemens Healthineers Company and the fruitful discussions with the ‘HollandPTC consortium – Erasmus Medical Center, Rotterdam, Holland Proton Therapy Centre, Delft, Leiden University Medical Center (LUMC), Leiden and Delft University of Technology, Delft, The Netherlands’.

The authors declare that they have no known competing financial interests or personal relationships that could have appeared to influence the work reported in this paper. Moreover, no data was used for the research described in the article.

## 9 CRediT statement

**Tiberiu Burlacu:** Conceptualization, methodology, software, validation, formal analysis, data curation, investigation, writing - original draft, writing - review & editing, visualization.

**Danny Lathouwers:** Conceptualization, methodology, software, validation, resources, writing - review & editing, supervision.

**Zoltán Perkó:** Conceptualization, methodology, validation, resources, writing - review & editing, supervision, project administration, funding acquisition.

## References

- [1] L. Zheng-Ming, A. Brahme, An overview of the transport theory of charged particles, *Radiation Physics and Chemistry* 41 (4) (1993) 673–703. doi:10.1016/0969-806X(93)90318-0.
- [2] J. J. Duderstadt, W. R. Martin, *Transport Theory*, New York, 1979.
- [3] P. Botas, J. Kim, B. Winey, H. Paganetti, Online adaption approaches for intensity modulated proton therapy for head and neck patients based on cone beam CTs and Monte Carlo simulations, *Physics in Medicine & Biology* 64 (1) (2018) 015004. doi:10.1088/1361-6560/aaf30b.
- [4] M. C. Cordaro, M. S. Zucker, The application of the phase space time evolution method to electron shielding, 1972.
- [5] H. Paganetti (Ed.), *Proton Therapy Physics*, CRC Press, Boca Raton, 2016. doi:10.1201/9780367803551.
- [6] A. J. Lomax, Intensity modulated proton therapy and its sensitivity to treatment uncertainties 1: The potential effects of calculational uncertainties, *Physics in Medicine and Biology* 53 (4) (2008) 1027–1042. doi:10.1088/0031-9155/53/4/014.
- [7] Z. Perkó, S. R. van der Voort, S. van de Water, C. M. H. Hartman, M. Hoogeman, D. Lathouwers, Fast and accurate sensitivity analysis of IMPT treatment plans using Polynomial Chaos Expansion, *Physics in Medicine and Biology* 61 (12) (2016) 4646–4664. doi:10.1088/0031-9155/61/12/4646.
- [8] H. Paganetti, Range uncertainties in proton therapy and the role of Monte Carlo simulations, *Physics in Medicine and Biology* 57 (11) (2012) R99–R117. doi:10.1088/0031-9155/57/11/R99.
- [9] J. Rojo-Santiago, S. J. M. Habraken, D. Lathouwers, A. Méndez Romero, Z. Perkó, M. S. Hoogeman, Accurate assessment of a Dutch practical robustness evaluation protocol in clinical PT with pencil beam scanning for neurological tumors, *Radiotherapy and Oncology: Journal of the European Society for Therapeutic Radiology and Oncology* 163 (2021) 121–127. doi:10.1016/j.radonc.2021.07.028.
- [10] S. van der Voort, S. van de Water, Z. Perkó, B. Heijmen, D. Lathouwers, M. Hoogeman, Robustness Recipes for Minimax Robust Optimization in Intensity Modulated Proton Therapy for Oropharyngeal Cancer Patients, *International Journal of Radiation Oncology, Biology, Physics* 95 (1) (2016) 163–170. doi:10.1016/j.ijrobp.2016.02.035.
- [11] J. Unkelbach, H. Paganetti, Robust Proton Treatment Planning: Physical and Biological Optimization, *Seminars in Radiation Oncology* 28 (2) (2018) 88–96. doi:10.1016/j.semradonc.2017.11.005.
- [12] H. Paganetti, P. Botas, G. C. Sharp, B. Winey, Adaptive proton therapy, *Physics in Medicine & Biology* 66 (22) (2021) 22TR01. doi:10.1088/1361-6560/ac344f.
- [13] S. van de Water, I. van Dam, D. R. Schaart, A. Al-Mamgani, B. J. M. Heijmen, M. S. Hoogeman, The price of robustness; impact of worst-case optimization on organ-at-risk dose and complication probability in intensity-modulated proton therapy for oropharyngeal cancer patients, *Radiotherapy and Oncology: Journal of the European Society for Therapeutic Radiology and Oncology* 120 (1) (2016) 56–62. doi:10.1016/j.radonc.2016.04.038.
- [14] C. Men, X. Jia, S. B. Jiang, GPU-based ultra-fast direct aperture optimization for online adaptive radiation therapy, *Physics in Medicine and Biology* 55 (15) (2010) 4309–4319. doi:10.1088/0031-9155/55/15/008.
- [15] A. Barrett, S. Morris, J. Dobbs, T. Roques, *Practical Radiotherapy Planning*, CRC Press, 2009.
- [16] M. Schwarz, Treatment planning in proton therapy, *The European Physical Journal Plus* 126 (2011) 1–10. doi:10.1140/epjp/i2011-11067-y.

- [17] B. Gottschalk, Passive Beam Spreading in Proton Radiation Therapy, draft Edition, Harvard High Energy Physics Laboratory, 2004.
- [18] S. J. Frank, X. R. Zhu, Proton Therapy Indications, Techniques, and Outcomes, 2020.
- [19] H. Li, N. Sahoo, F. Poenisch, K. Suzuki, Y. Li, X. Li, X. Zhang, A. K. Lee, M. T. Gillin, X. R. Zhu, Use of treatment log files in spot scanning proton therapy as part of patient-specific quality assurance, *Medical Physics* 40 (2) (2013) 021703. doi:10.1118/1.4773312.
- [20] G. Meier, R. Besson, A. Nanz, S. Safai, A. J. Lomax, Independent dose calculations for commissioning, quality assurance and dose reconstruction of PBS proton therapy, *Physics in Medicine and Biology* 60 (7) (2015) 2819–2836. doi:10.1088/0031-9155/60/7/2819.
- [21] A. Meijers, G. Guterres Marmitt, K. Ng Wei Siang, A. van der Schaaf, A. C. Knopf, J. A. Langendijk, S. Both, Feasibility of patient specific quality assurance for proton therapy based on independent dose calculation and predicted outcomes, *Radiotherapy and Oncology: Journal of the European Society for Therapeutic Radiology and Oncology* 150 (2020) 136–141. doi:10.1016/j.radonc.2020.06.027.
- [22] M. Matter, L. Nenoff, G. Meier, D. C. Weber, A. J. Lomax, F. Albertini, Alternatives to patient specific verification measurements in proton therapy: A comparative experimental study with intentional errors., *Physics in medicine and biology* 63 (20) (2018) 205014. doi:10.1088/1361-6560/aae2f4.
- [23] O. Pastor-Serrano, Z. Perkó, Millisecond speed deep learning based proton dose calculation with Monte Carlo accuracy, *Physics in Medicine & Biology* 67 (10) (2022) 105006. doi:10.1088/1361-6560/ac692e.
- [24] L. Eyges, Multiple Scattering with Energy Loss, *Physical Review* 74 (10) (1948) 1534–1535. doi:10.1103/PhysRev.74.1534.
- [25] A. Brahme, Simple relations for the penetration of high energy electron beams in matter, Tech. rep., Sweden (1975).
- [26] C. Börgers, The Radiation Therapy Planning Problem, in: W. Miller, C. Börgers, F. Natterer (Eds.), *Computational Radiology and Imaging*, Vol. 110, Springer New York, New York, NY, 1999, pp. 1–16. doi:10.1007/978-1-4612-1550-9\_1.
- [27] J. Duderstadt, L. Hamilton, *Nuclear Reactor Analysis*, Wiley, 1991.
- [28] T. Gebäck, M. Asadzadeh, Analytical Solutions for the Pencil-Beam Equation with Energy Loss and Straggling, *Transport Theory and Statistical Physics* 41 (5-6) (2012) 325–336. doi:10.1080/00411450.2012.671207.
- [29] D. Cacuci, *Sensitivity and Uncertainty Analysis, Volume I: Theory*, Vol. 1, 2003. doi:10.1201/9780203498798.
- [30] B. Rivière, *Discontinuous Galerkin Methods for Solving Elliptic and Parabolic Equations*, *Frontiers in Applied Mathematics*, Society for Industrial and Applied Mathematics, 2008. doi:10.1137/1.9780898717440.
- [31] E. Suli, D. F. Mayers, *An Introduction to Numerical Analysis* 444.
- [32] A. Gerbershagen, A. Adelman, R. Dölling, D. Meer, V. Rizzoglio, J. Schippers, Simulations and measurements of proton beam energy spectrum after energy degradation, *Journal of Physics: Conference Series* 874 (2017) 012108. doi:10.1088/1742-6596/874/1/012108.
- [33] K. Hillewaert, Development of the discontinuous Galerkin method for high-resolution, large scale CFD and acoustics in industrial geometries, Ph.D. thesis, UCL - Université Catholique de Louvain (2013).

- [34] E. Anderson, Z. Bai, C. Bischof, S. Blackford, J. Demmel, J. Dongarra, J. Du Croz, A. Greenbaum, S. Hammarling, A. McKenney, D. Sorensen, LAPACK Users' Guide, 3rd Edition, Society for Industrial and Applied Mathematics, Philadelphia, PA, 1999.
- [35] D. Jette, Electron dose calculation using multiple-scattering theory. A. Gaussian multiple-scattering theory., *Medical physics* 15 (2) (1988 Mar-Apr) 123–137. doi:10.1118/1.596166.
- [36] B. Gottschalk, Techniques of Proton Radiotherapy: Transport Theory (2012). doi:10.48550/ARXIV.1204.4470.
- [37] R. Piessens, E. deDoncker-Kapenga, C. Ueberhuber, D. Kahaner, QUADPACK: A Subroutine Package for Automatic Integration, Springer (1983).
- [38] W. Schneider, T. Bortfeld, W. Schlegel, Correlation between CT numbers and tissue parameters needed for Monte Carlo simulations of clinical dose distributions, *Physics in Medicine and Biology* 45 (2) (2000) 459–478. doi:10.1088/0031-9155/45/2/314.
- [39] J. Perl, J. Shin, J. Schumann, B. Faddegon, H. Paganetti, TOPAS: An innovative proton Monte Carlo platform for research and clinical applications, *Medical Physics* 39 (11) (2012) 6818–6837. doi:10.1118/1.4758060.
- [40] J. Schuemann, H. Paganetti, Stopping power extraction.
- [41] H. Noshad, S. S. Bahador, Investigation on energy straggling of protons via Fokker–Planck equation, *Nuclear Instruments and Methods in Physics Research Section B: Beam Interactions with Materials and Atoms* 288 (2012) 89–93. doi:10.1016/j.nimb.2012.07.030.
- [42] E. J. Williams, W. L. N. Bragg, The passage of  $\alpha$ - and  $\beta$ - particles through matter and Born's theory of collisions, *Proceedings of the Royal Society of London. Series A, Containing Papers of a Mathematical and Physical Character* 135 (826) (1932) 108–131. doi:10.1098/rspa.1932.0023.
- [43] H. Goldstein, C. P. J. Poole, J. Safko, Classical Mechanics, 3rd Edition, Addison-Wesley, Reading, Mass., 2002.
- [44] E. Sundermann, F. Jacobs, M. Christiaens, B. De Sutter, I. Lemahieu, A Fast Algorithm to Calculate the Exact Radiological Path Through a Pixel Or Voxel Space, *Journal of Computing and Information Technology* 6.
- [45] T. Bortfeld, An analytical approximation of the Bragg curve for therapeutic proton beams, *Medical Physics* 24 (12) (1997) 2024–2033. doi:10.1118/1.598116.
- [46] M. Soukup, M. Fippel, M. Alber, A pencil beam algorithm for intensity modulated proton therapy derived from Monte Carlo simulations, *Physics in Medicine and Biology* 50 (21) (2005) 5089–5104. doi:10.1088/0031-9155/50/21/010.
- [47] J. Yang, P. He, H. Wang, G. Sun, H. Zheng, J. Jia, An improved beam splitting method for intensity modulated proton therapy, *Physics in Medicine & Biology* 65 (18) (2020) 185015. doi:10.1088/1361-6560/ab9b55.